Auxin-driven ecophysiological diversification of leaves in domesticated tomato

Juliene d. R. Moreira[1]; Bruno L. Rosa[1]; Bruno S. Lira[2]; Joni E. Lima[3]; Ludmila N. Souza[1]; Wagner C. Otoni[1]; Antonio Figueira[4]; Luciano Freschi[2]; Tetsu Sakamoto[5]; Lázaro E. P. Peres[6]; Magdalena Rossi[2]; Agustin Zsögön[1]

[1]*Departamento de Biologia Vegetal, Universidade Federal de Viçosa, 36570-900, Viçosa, MG, Brazil*

[2]*Departamento de Botânica, Instituto de Biociências, Universidade de São Paulo, 05508-090, São Paulo, SP, Brazil*

[3]*Departamento de Botânica, Instituto de Ciências Biológicas, Universidade Federal de Minas Gerais, 31270-901, Belo Horizonte, MG, Brazil*

[4]*Centro de Energia Nuclear na Agricultura, Universidade de São Paulo, 13400-970, Piracicaba, São Paulo, Brazil*

[5]*Bioinformatics Multidisciplinary Environment, Instituto Metrópole Digital, Universidade Federal Do Rio Grande Do Norte, Natal, RN, Brazil*

[6]*Laboratory of Hormonal Control of Plant Development. Departamento de Ciências Biológicas (LCB), Escola Superior de Agricultura "Luiz de Queiroz", Universidade de São Paulo, CP 09, 13418-900, Piracicaba, SP, Brazil*

Corresponding author

Agustin Zsögön
Universidade Federal de Viçosa, Brazil
Phone: +55 31 3899 2592
Fax: +55 31 3899 4139
Email: agustin.zsogon@ufv.br

One sentence summary: Distribution of heterobaric and homobaric leaves is controlled by natural variation in an auxin-related transcription factor

Summary

The study of crop diversification has focussed mainly on the genetic changes underlying traits favoured by humans. However, the passage from natural habitats to agronomic settings probably operated changes beyond those comprising the classical domestication syndrome. A deeper understanding of these traits and their genetic signature would be valuable to inform conventional crop breeding and *de novo* domestication of crop wild relatives. Heterobaric leaves have bundle sheath extensions (BSEs) that compartmentalise the sub-stomatal cavity whereas homobaric leaves do not; BSE development is known to be controlled by the *OBSCURAVENOSA* (*OBV*) locus and the *obv* mutant lacks BSEs whereas leaves carrying the wild type allele have BSEs. Here we identify the *OBV* gene and the causative mutation, a non-synonymous amino acid change. This mutation exists as a rare balanced polymorphism in the natural range of wild tomatoes, but has increased in frequency in domesticated tomatoes suggesting that the latter diversified into heterobaric and homobaric leaf types. The mutation disrupts a C2H2 zinc finger motif in the OBV protein, resulting in the absence of BSEs in leaves and here we show that this and other pleiotropic effects, including changes in leaf insertion angle, leaf margin serration, minor vein density and fruit shape, are controlled by OBV via changes in auxin signalling. Loss of function of the transcriptional regulator AUXIN RESPONSE FACTOR (ARF4) also results in defective BSE development, revealing an additional component of a novel genetic module controlling aspects of leaf development important for ecological adaptation and subject to breeding selections.

Crop domestication was driven by artificial selection to create a loose suite of traits known as the 'domestication syndrome' (*1*). Considerable effort has been devoted to unveiling the genetic basis of the domestication syndrome traits. However, the passage from natural ecosystems to increasingly sophisticated, human-managed ones created new drivers for crop evolution that may have had impact beyond the domestication syndrome (*2*). These drivers include geographic expansion beyond the crops' centre of origin, natural selection under cultivation in a highly managed environment, and indirect selection due to constraints caused by developmental trait correlations and physiological trade-offs (*3*). The extent and breadth of the genetic signature created by those processes in crops is not yet known. Identifying such genetic variants and characterizing their consequences to plant development and function would lead to a more integrated understanding of crop ecology and provide valuable support to crop breeding and to the effort of creating new crops with *de novo* domestication pipelines (*4*, *5*).

Leaf functional traits are key for resource acquisition and thus strongly constrained by developmental co-variation (*6*). For instance, high photosynthetic rates require high transpiration capacity, which in turn depends on water transport capacity (*7*). Leaf hydraulic conductance is a fundamental driver of leaf diversity, as it is linked with leaf shape, longevity and venation architecture (*8*). Notably, many angiosperm species have translucent leaf veins due to the presence of bundle sheath extensions (BSEs), compact columns of chlorophyll-less cells that link the veins to the leaf epidermis (*9*, *10*) (Fig. 1A). BSEs have considerable functional impact, as they can divide the leaf mesophyll into compartments, resulting in patchy stomatal opening and non-uniform photosynthesis (*11*). Leaves harbouring such compartments created by BSEs are called heterobaric, as opposed to homobaric ones, where the leaf lamina is topologically continuous. The effect of BSEs on leaf compartmentalization can be demonstrated by water infiltration in the lamina (*12*). The distribution of these leaf functional types in natural ecosystems is highly skewed: in a climax forest, most species from the upper strata are heterobaric, whereas those dwelling in the understorey are homobaric (*13*). Likewise, some crops (*e.g.* soybean, sunflower) are heterobaric, whereas others (*e.g.* coffee, cacao) are homobaric (*14*). What determines the distribution of these leaf functional types in natural and agricultural environments? Identifying the genetic basis of BSEs development would provide a stepping stone to answer this question.

90 We previously reported that the tomato monogenic recessive mutant *obscuravenosa*
91 (*obv*) lacks BSEs in leaves, leading to reduced water transport capacity: both stomatal
92 conductance (g_s) and hydraulic conductance (K_{leaf}) are lower in the mutant compared to wild-
93 type (WT) plants (*15*). Analysis of *S. pennellii* introgression lines (ILs) in tomato showed
94 that *OBV* resides on a chromosome 5 interval defined by the bin d-5E (Fig. 1B and C), which
95 contains 37 genes (Table S1) (*16*). A genome wide association study (GWAS) using 25 wild-
96 type and 12 *obv* mutant accessions revealed a significant single nucleotide polymorphism
97 (SNP) in Solyc05g054030 (Fig. 1D and fig. S1). The SNP is an A→G nucleotide change in
98 the third exon of the gene coding sequence (CDS), resulting in a predicted histidine to
99 arginine substitution on position 135 (H135R) of the protein (Fig. 1E), which is present in
100 different tomato cultivars harbouring the *obv* mutation (Table S2). This genetic identity for
101 *obv* was reported recently during the preparation of this manuscript (*17*). Combining genomic
102 and passport information we analysed the geographic distribution of the mutation in the
103 natural range of tomato wild relatives, including the ancestral species *S. pimpinellifolium* and
104 found a sympatric cluster of mutant accessions in the lowlands of Ecuador and northern Peru
105 (Fig. 1F). Nucleotide diversity analysis on 360 wild and domesticated tomato accessions
106 (available on solgenomics.net) showed that *OBV* resides within a tomato domestication
107 sweep (Fig. 1G) (*18*). We also found that the mutation increases in frequency between
108 accessions along the wild-domesticated continuum (Fig. 1H).

109 To confirm the genetic identity of *OBV*, we transformed the *obv* mutant in tomato cv.
110 Micro-Tom (MT-*obv*) (Figure 2A) with an overexpression (OE) vector for the CDS of
111 Solyc05g054030. We observed correct BSE development leading to translucent veins in all
112 *obv* plants harbouring the construct (Fig. 2B, and fig. S2). To assess whether the defect in
113 BSE development in *obv* is indeed caused by a single, non-synonymous nucleotide change
114 we constructed another OE vector with the *OBV* CDS but containing a A404G SNP and
115 transformed it into the *obv* mutant. All lines expressed the transgene, but none reverted the
116 dark-vein mutant phenotype lacking BSEs (Fig. 2C and fig. S3). We further confirmed that
117 the *obv* mutant could be phenocopied by knocking down Solyc05g054030 expression with
118 an RNA interference (RNAi) construct (Fig. 2D). We further crossed two homobaric
119 cultivars (M82 and VFN8) with either the *obv* mutant in the MT background or the *obv*
120 mutant complemented with the *OBV*-OE transgene (MT-*obv* OBV^{OE}). Hybrid plants derived

121 from M82 × MT-*obv* or VFN8 × MT-*obv* lacked BSEs leading to dark veins, but those
122 derived from the cross with MT-*obv* OBV^{OE} showed phenotypic reversion, displaying
123 translucent veins and BSEs (Fig. 2E and fig. S4). These results demonstrated that
124 Solyc05g054030 is *OBV*, the gene responsible for BSE development in tomato leaves, and
125 that a single amino acid change causes the *obv* mutation, which is responsible for the switch
126 from heterobaric to homobaric leaves in tomato (*14*).

127 To better understand the nature of the genetic change underlying the *obv* mutation,
128 we conducted *in silico* analyses of the gene and protein sequences of *OBV* (Fig. 2F). The
129 complete sequence of the *OBV* gene encodes a 381 amino acid protein containing three Cys_2-
130 Hys_2 (C2H2) Zn finger domains, which are associated with DNA-binding capability (*19*), an
131 ethylene-responsive element binding factor-associated amphiphilic repression (EAR)
132 domain, defined by the LxLxL motif and associated with transcriptional repression (*20*), and
133 a carboxy-terminal coiled coil domain, which may function as molecular spacer or
134 macromolecular scaffold (*21*). Gene ontology (GO) terms associated with this protein are
135 nucleic acid binding (GO:0003676) and metal ion binding (GO:0046872) (Table S2). Using
136 324 protein sequences of the *OBV* orthologous group from 39 plant species (Table S3) we
137 identified the H135R amino acid change of the *obv* mutant to a highly conserved motif of the
138 second Zn finger domain (Fig. 2G). Protein modelling showed that the C2H2 motif is
139 contained within a ββα structure, forming a functional unit stabilized internally by chelation
140 of a single zinc ion (Fig. 2F). This suggests that the *obv* mutation leads to complete loss of
141 protein function via disruption of its tertiary structure. Targeted phylogenetic analysis in
142 relevant crop and model species revealed an ancient evolutionary origin of the *OBV* gene
143 with great expansion due to duplication events (Fig. 2G and fig. S6). Protein sequence
144 alignment of the Zn finger motif that contains the *obv* mutation in tomato showed that even
145 the most phylogenetically distant species displayed high sequence identity across the domain,
146 suggesting a conserved protein function (Fig. 2G). The closest *Arabidopsis* orthologs
147 (*INDETERMINATE DOMAIN 14*, *15* and *16*), encode proteins involved in shoot
148 gravitropism and regulation of auxin biosynthesis and transport (Table S4 and fig. S6) (*22*).

149 We next characterized the expression profile of *OBV*: the gene is highly expressed in
150 meristems leaf primordia, expanding and mature leaves and flowers (fig. S7A and B).
151 Increased *OBV* expression levels in transgenic plants led to changes on leaf insertion angle,

152 leaf margin serration and fruit shape (fig. S7C-E), which hinted at a potential role for auxin
153 as a mediator of BSE development. Auxins, like other plant hormones, exert their effect
154 through alterations in metabolism, transport, and sensitivity (*23*). We found no differences
155 either in auxin content (fig. S9A) nor in polar auxin transport (fig. S9B) between wild type,
156 *obv* mutant and *OBV*^{OE} lines in leaf primordia. However, GUS expression driven by the *DR5*
157 auxin-induced promoter was increased in the *obv* mutant (Fig. 3A) but decreased in the
158 *OBV*^{OE} lines (fig. S10). All the lines responded to exogenous auxin application with high
159 *GUS* expression (Fig. 3A and fig. S10). Exogenous auxin application also led to higher
160 inhibition of hypocotyl elongation and stimulation of *in vitro* rhizogenesis in *obv* explants,
161 compared to WT or *OBV*^{OE} lines (fig. S11). Taken together, the results suggested that *OBV*
162 could be responsible for changes in auxin signalling. Thus, we assessed the expression
163 profiles of *AUXIN RESPONSE FACTOR* (*ARFs*) and *AUXIN/INDOLE-3-ACETIC ACID*
164 (*Aux/IAAs*) transcriptional regulators, which are components of auxin signal transduction
165 (*24*). We found consistent upregulation of some *ARFs* (*ARF3*, *9B*, *10B*, *19* and *AUX/IAA4*
166 and *14*) and downregulation of some *Aux/IAAs* (*Aux/IAA1A*, *1B*, *2*, *3*, *11*, *13*, *26* and *35*) in
167 *OBV*^{OE} lines compared to WT (Fig. 3B). Regarding *obv*, expression differences were found
168 for *ARF4* and *Aux/IAA15*, both of which were clearly upregulated in the *obv* mutant compared
169 to WT (Fig. 3B).

170 We then tested the potential role of *ARF4* in BSE development using a CRISPR/Cas9-
171 generated knockout mutant (*arf4*-CR) and a transcriptionally silenced line harbouring an
172 *ARF4*-antisense (*ARF4*-as) transgene (*25*). We confirmed the lack of BSEs and the associated
173 dark vein phenotype in leaves of both *arf4-CR* and *ARF4*-as plants (Fig. 3C and fig S11).
174 Further, *OBV* expression was not altered in *arf4* and *ARF4-as* leaves (Fig. 3D) but increased
175 four-fold in the *obv* mutant, suggesting the existence of a hypothetical negative feedback
176 mechanism at the transcriptional level. *ARF4* expression was increased in the *obv* mutant but
177 not in the *OBV*^{OE} lines (Fig. 3E). Taken together, these results suggest that *OBV* controls BSE
178 development via interaction with the auxin signalling machinery.

179 As *OBV* modulates auxin sensitivity and signaling, we tested whether allelic variation
180 in *OBV* also determines the link between leaf structure and function. We first determined that
181 leaf vein density (vein length per leaf area, VLA) was reduced in *obv* plants (Fig 4A and B).
182 Vein architecture plays a key role in carbon assimilation rate and water distribution within

183 the leaf (*26*). K_{leaf} is a measure of how efficiently water is transported through the leaf: We
184 found that the *obv* mutant showed reduced K_{leaf}, which was restored to wild-type levels in
185 OBV^{OE} complemented lines (Fig. 4C). A regression analysis between VLA and K_{leaf} showed
186 a strong positive correlation (r=0.811, p<0.001), with a coefficient of determination (R^2) of
187 0.657 (Fig. 4D). This suggests that variation in VLA caused by *OBV* is a major determinant
188 of variation in K_{leaf}. Interestingly, an auxin biosynthesis mutant with reduced VLA showed
189 reduced K_{leaf} and photosynthetic rate in pea (*Pisum sativum*) (*27*). Net assimilation of CO_2
190 (A_n)-chloroplastic CO_2 concentration curves (C_c) (Fig. 4E) revealed no difference in
191 maximum Rubisco carboxylation rate (V_{cmax}) (Table S6) between genotypes. However, the
192 maximum rate of light-saturated net CO_2 assimilation (A_{max}) was lower in the *obv* mutant
193 (Fig. 4E and F and Table S7). This suggests that the presence of BSEs overrides diffusive
194 limitations to photosynthesis through their effect on the water transport capacity of the plants
195 (*28*, *29*).

196 Leaf BSEs fulfill significant roles in leaf function with large ecophysiological impact.
197 Firstly, by connecting the vascular bundles to the leaf epidermis, BSEs minimize the extra-
198 xylematic path length and favor a greater hydraulic integration in the leaf lamina. The stomata
199 of heterobaric leaves may therefore operate closer to the point of embolism, while responding
200 faster to sudden changes in xylem water potential (*30*). To some extent, this could explain
201 the distribution of heterobaric wild tomato accessions in more arid habitats with erratic
202 rainfall patterns (*31*). Secondly, photosynthetic assimilation rates are higher in heterobaric
203 leaves due to the optimization of light transmission within the leaf lamina. BSEs can function
204 as 'transparent windows' that enrich neighbouring mesophyll cells, or, in the case of C_4
205 plants, the bundle sheath itself, with high levels of photosynthetically active radiation (400-
206 700 nm) (*32*, *33*). Lastly, the presence of BSEs increases the plasticity of minor vein density
207 in response to growth light intensity, adjusting water supply and photosynthetic rate to
208 specific environmental conditions (*12*). The sum of these effects on leaf function suggests
209 that the presence of BSEs has adaptive value. This raises the question of what the main driver
210 for the loss of BSEs in many domesticated tomato cultivars could be. One possible
211 explanation is that the heterobaric/homobaric ecological distribution logic was broken down
212 by the transition to an agricultural setting and, in this case, the homobaric phenotype is
213 functionally more advantageous due a trade-off with the structural and functional costs of

214 BSEs (*34*). Furthermore, since the *obv* mutation increases sensitivity to auxin, we cannot
215 exclude the selection of a favorable pleiotropic effect of this hormone on plant development
216 and productivity (*35*).

217 In this report we have identified an allelic variant in *OBV*, a gene controlling the
218 development of BSEs, which impacts leaf anatomy and function in tomato and other
219 important crop species. We show that the OBV protein is highly conserved among
220 angiosperms and that it is a key determinant of leaf functional type. BSE development is
221 strongly linked to auxin signalling, involving *ARF4*, whose loss of function also impairs BSE
222 formation. Our findings represent an entry point to unravel leaf functional design through a
223 gene-focused approach and provide a molecular anchor for the analysis of phenotypic co-
224 variation in leaf anatomical and physiological traits. Our results also suggest that leaf
225 functional type results from a trade-off probably conditioned by environmental factors. The
226 conservation of *OBV* in angiosperms could be leveraged to explore its roles in other plant
227 major crop species and potentially tailor different leaf types to specific agronomic settings.
228 For instance, BSEs were recently shown to provide a pathway for P uptake following foliar
229 fertilization in spring barley (*Hordeum vulgare*) (*36*). Thus, our discovery of a simple genetic
230 switch between leaf functional types could have important ecological implications and
231 agricultural applications.

232

233 **Figures**

234

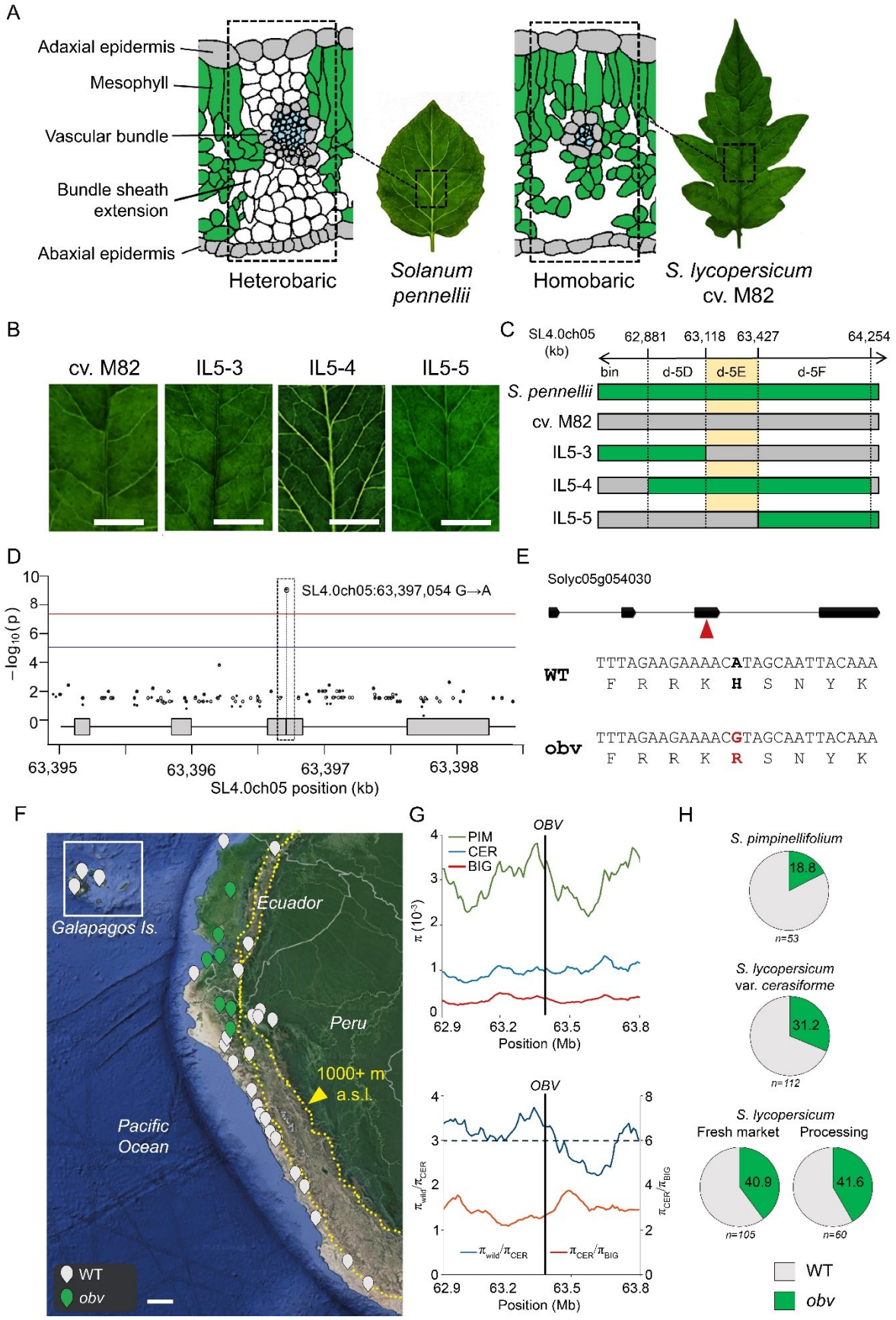
A
Adaxial epidermis
Mesophyll
Vascular bundle
Bundle sheath extension
Abaxial epidermis
Heterobaric
Solanum pennellii
Homobaric
S. lycopersicum cv. M82
B
cv. M82
IL5-3
IL5-4
IL5-5
C
SL4.0ch05 (kb)
62,881
63,118
63,427
64,254
bin
d-5D
d-5E
d-5F
S. pennellii
cv. M82
IL5-3
IL5-4
IL5-5
D
SL4.0ch05:63,397,054 G→A
−log10(p)
63,395
63,396
63,397
63,398
SL4.0ch05 position (kb)
E
Solyc05g054030
WT
TTTAGAAGAAAACATAGCAATTACAAA
F R R K H S N Y K
obv
TTTAGAAGAAAACGTAGCAATTACAAA
F R R K R S N Y K
F
Galapagos Is.
Ecuador
Peru
1000+ m a.s.l.
Pacific Ocean
WT
obv
G
PIM
CER
BIG
OBV
π (10⁻³)
Position (Mb)
π_wild/π_CER
π_CER/π_BIG
H
S. pimpinellifolium
18.8
n=53
S. lycopersicum var. cerasiforme
31.2
n=112
S. lycopersicum
Fresh market
Processing
40.9
41.6
n=105
n=60
WT
obv

235

236 **Figure 1 – Mapping and identification of a candidate gene for the *obscuravenosa* (*obv*) mutation.** (**A**)
237 Schematic cross-sectional comparison of heterobaric and homobaric leaves. In the heterobaric leaves (*e.g.* the
238 tomato wild relative *Solanum pennellii*) the bundle sheath extensions (BSEs) are visible as a translucent network
239 of veins, whereas in homobaric leaves (*e.g.* cultivars of tomato, *S. lycopersicum*, harbouring the *obv* mutation,
240 such as cv. M82) the leaf lamina appears uniformly green. (**B**) Leaf phenotype of tomato cv. M82 and the *S.*
241 *pennellii* introgression lines (IL) 5-3, 5-4 and 5-5. Scale bars, 1 cm. (**C**) Bin-mapping of the genomic region
242 containing the *obv* mutation using ILs sequences. (**D**) Association plot of the Genome-Wide Association Study
243 (GWAS) for the *obv* phenotype: the x-axis represents the chromosome region where Solyc05g054030 is
244 located, and the y-axis represents the negative $\log_{10}$ of *p*-values per SNP derived from the association analysis.
245 The red horizontal line represents the Bonferroni-corrected genome-wide significance threshold (p=1.554^{-08}).
246 The boxes represent the open reading frame of Solyc05g054030. The SNP (an A-to-G transition) located in the
247 third exon of Solyc05g054030 is strongly associated with the *obv* phenotype. (**E**) Gene structure of
248 Solyc05g054030 showing exons (boxes) and introns (lines) and the position of the SNP (red arrowhead) in the
249 third exon and DNA and amino acid sequence of the region around the SNP, showing that it represents a non-
250 synonymous mutation leading to the substitution of a Histidine (H) in the wild-type (WT) for an Arginine (R)
251 in the *obv* mutant. (**F**) Geographic distribution of accessions of wild tomatoes on the Pacific coast of Peru,
252 Ecuador and the Galapagos Islands (inset) harbouring either the WT or mutant *obv* allele. Scale bar, 100 km.
253 (**G**) Nucleotide diversity (π) of the ancestral wild species *S. pimpinellifolium* (PIN), *S. lycopersicum* var.
254 *cerasiforme* (CER) and big-fruit cultivars (BIG) of domesticated tomato. The horizontal lines indicates genome-
255 wide top 5% cutoff ratio for domestication sweeps. (**H**) Frequency of the *obv* mutation in four different
256 categories of tomato accessions (*S. pimpinellifolium; S. lycopersicum* var. *cerasiforme; S. lycopersicum* fresh
257 or processing cultivars).

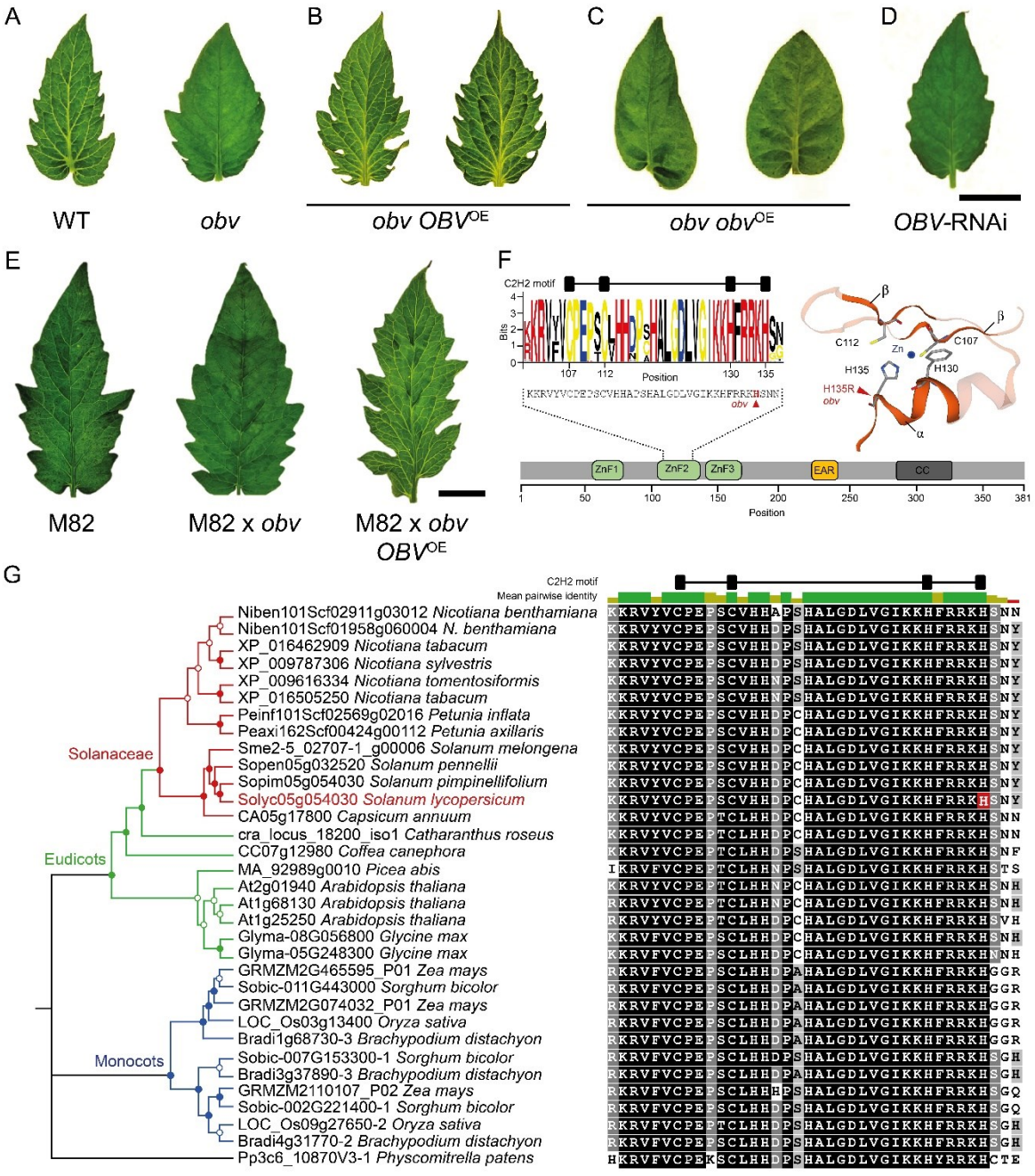

Figure 2 – Complementation of the *obv* mutant and protein sequence analysis. (**A**) Representative terminal leaflets of tomato cultivar Micro-Tom (MT) harbouring the wild-type (WT) *OBV* allele and the *obscuravenosa* (*obv*) mutant, (**B** and **C**) independent transgenic *obv* mutant lines overexpressing (OE) either (**B**) the WT *OBV* allele or (**C**) the mutant *obv* allele, and (**D**) an RNA interference knockdown *OBV* line in WT background. (**E**) Representative terminal leaflets of tomato cv. M82 (an *obv* mutant), an F_1 hybrid derived from the cross between M82 and MT-*obv* and an F_1 hybrid of M82 and transgenic MT-*obv* harbouring the *OBV* overexpression transgene. Scale bars, 1 cm. (**F**) Schematic representation of the *OBV* protein showing conserved domains: ZnF (zinc finger), EAR (ethylene-responsive element binding factor-associated amphiphilic repression) and CC (coiled coil). The sequence of the second ZnF motif (ZnF2) is described as logo plot of residue conservation, with consensus sequence in the bottom. The relative sizes of letters indicate their frequency in an orthologous

group of 324 proteins from 39 plant species. The total height of the letters depicts the information content of the position in bits. Right, 3D model of ZnF2 showing the relative positional arrangement of the C2H2 residues and the Zn ion ligand. (**G**) Left, maximum likelihood protein sequence tree of the *OBV* gene in selected model and crop species. Symbols on nodes represent bootstrap support values: full circles >0.75, open circles <0.75. Right, partial protein sequence alignment focused on the second ZnF and showing the Histidine (H) residue affected by the *obv* mutation in tomato (red). Shading indicates similarity to consensus (according to Blosum62 score matrix with a threshold of 1): black 100%; dark grey 80-99%; light grey 60-79%; white <60%. The bar on the top indicates the mean pairwise identity over all pairs in the column: green 100%; brown 30-99%, red <30%.

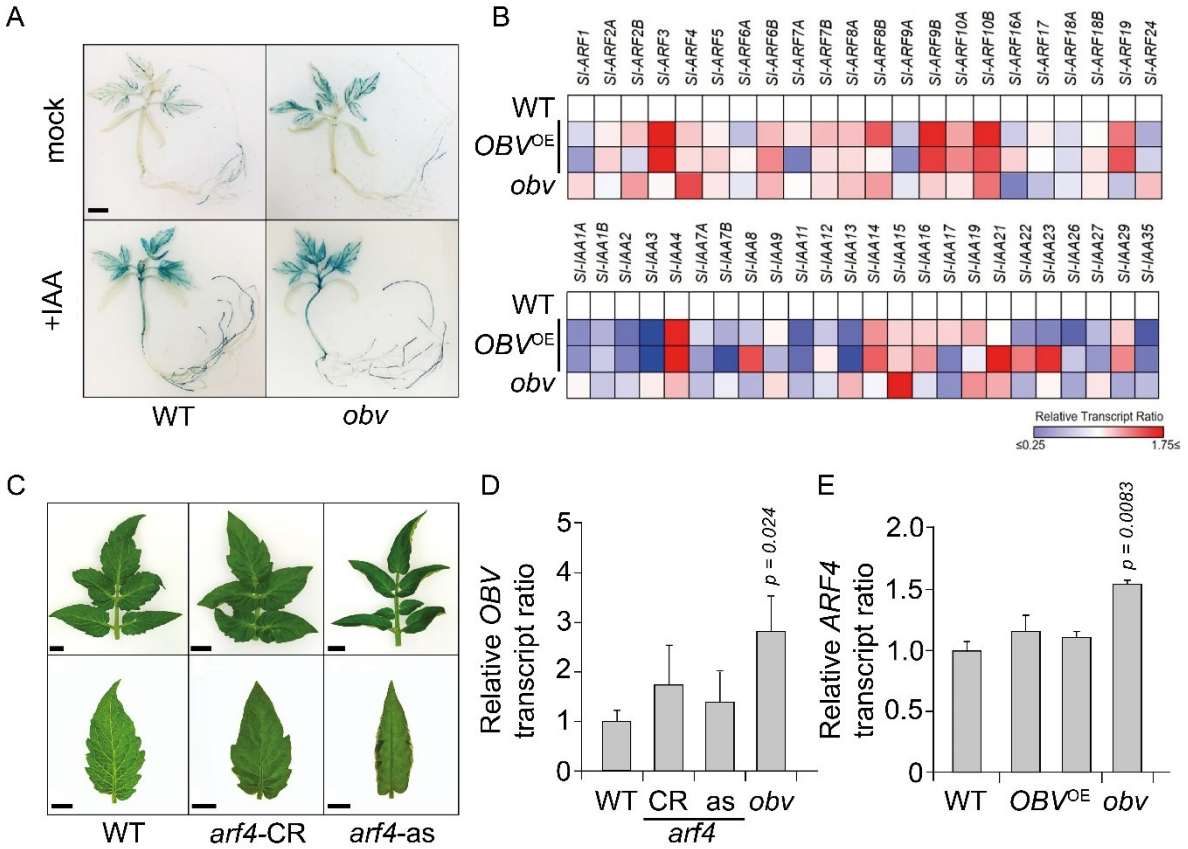

Figure 3 – Interaction between *OBV* and auxin signaling in the control of leaf functional type. (**A**) Histochemical GUS analysis in transgenic lines harbouring a homozygous *DR5*::*GUS* construct in either wild type (WT) Micro-Tom or *obv* mutant background. Seedlings were either pre-treated (+IAA) or not (mock) with 20 µM of indol-3-acetic acid (IAA). Scale bar = 1 cm. (**B**) Transcriptional profile of *AUXIN RESPONSE FACTOR* (*ARF*) and *AUXIN/INDOLE-3-ACETIC* (*Aux/IAA*) genes from leaf primordia. Heat map represents the transcript profiles in two *OBV* overexpression (OE) homozygous transgenic lines and the *obv* mutant. Values represent means of four biological replicates normalized against the corresponding WT sample. Statistically significant increases (red) or decreases (blue) in comparison with MT are represented by colored squares (p <0.05). (**C**) Representative leaves and terminal leaflets of MT, a CRISPR *ARF4* mutant (*arf4*-CR) and an antisense *ARF4* knockdown line (*arf4*-as). Scale bars = 1 cm. (**D**) Relative *OBV* mRNA levels in young leaves of MT, *arf4*-CR, *arf4*-as and *obv*. p-values show significant differences to the *obv* mutant. (**E**) Relative *ARF4* mRNA levels in young leaves of MT, homozygous transgenic lines overexpressing (OE) *OBV* and the *obv* mutant. p-values show significant differences to the *obv* mutant. Bars represent mean ± s.e.m. (n=4). A one-way analysis of variance (ANOVA) test compared the means, where significant (p<0.05), values are shown.

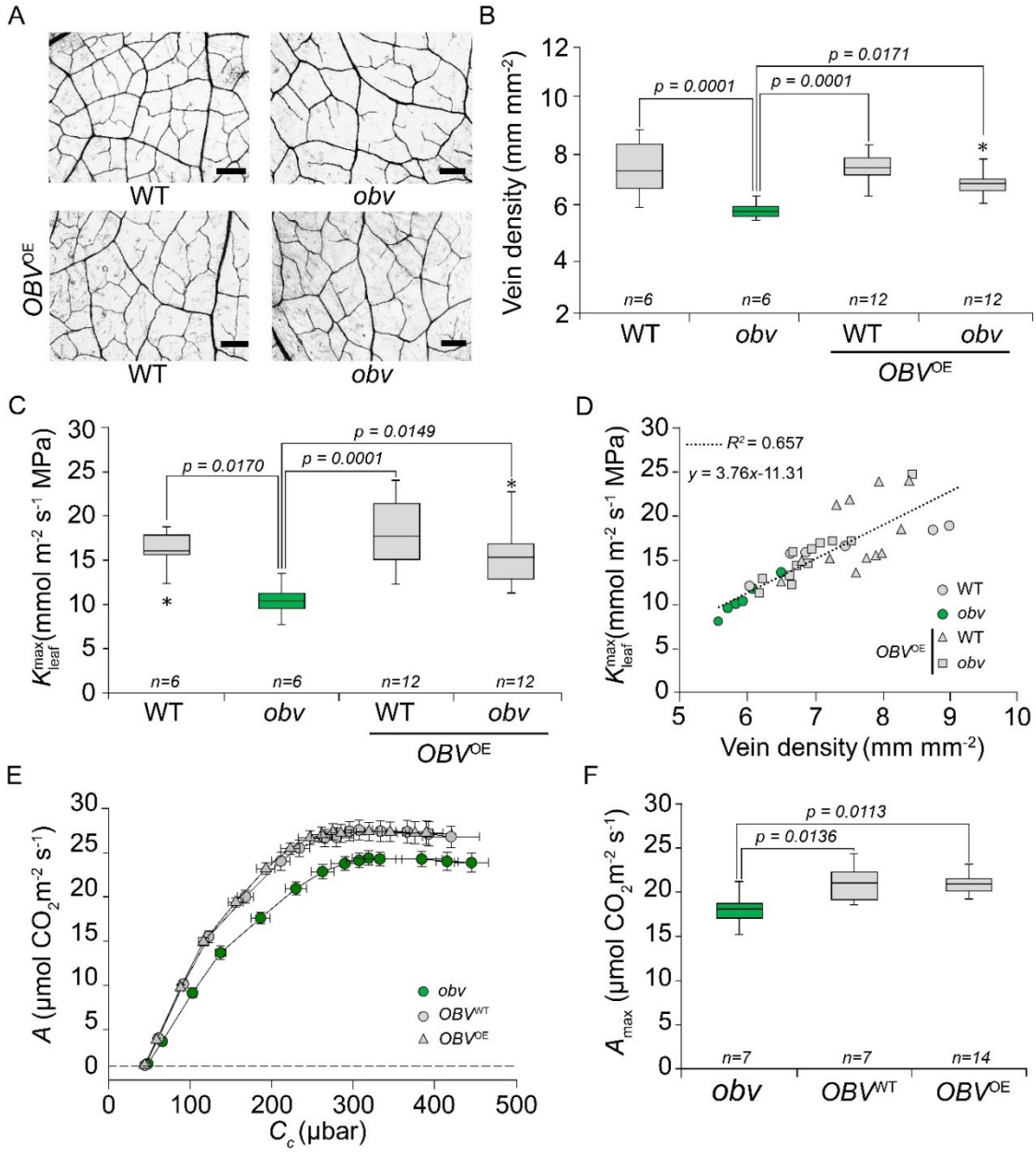

Figure 4 - *OBV* controls vein development and leaf hydraulic conductance for hydrated leaves (K_{leaf}^{max}). (**A**) Representative micrographs of cleared terminal leaflets of wild-type (WT) tomato cv. Micro-Tom (MT), the *obscuravenosa* (*obv*) mutant, and two independent *OBV* overexpression (OE) lines sections in either WT or *obv* background. Scale bars, 100 µm. (**B**) Leaf vein density in WT, *obv* and the transgenic lines. (**C**) values for tomato cv. M82 (*obv* mutant), a cv. M82 line harbouring the wild-type *OBV* allele introgressed by conventional breeding and a transgenic *OBV*-OE line; and (**D**) in WT, *obv* and the transgenic lines. (**E**) Regression analysis of K_{leaf}^{max} and vein density for WT, *obv* and the transgenic lines. Each point corresponds to an individual measurement on a different plant. (**F**) Net photosynthetic assimilation (A_n) response curve to CO_2 concentration in the chloroplasts (C_c), each point represents mean ± s.e.m. (n=8). (**G**) Maximum assimilation rate at ambient CO_2 and saturating irradiance derived from the curves in **F**. Boxes in box plots represent interquartile range (IQR), center line the mean, and the ends of the whisker are set at 1.5*IQR above and below the third and first quartiles, respectively. Asterisks show outliers. *p*-values for significant differences ($p<0.05$) are shown.

References

1. K. Hammer, *Die Kulturpflanze*. **32**, 11–34 (1984).
2. R. Milla, C. P. Osborne, M. M. Turcotte, C. Violle, *Trends in Ecology and Evolution*. **30**, 463–9 (2015).
3. R. Milla, J. Morente-López, J. M. Alonso-Rodrigo, N. Martín-Robles, F. S. Chapin, *Proceedings of the Royal Society B*. **281**, 20141429–20141429 (2014).
4. K. Gasparini, J. dos R. Moreira, L. E. P. Peres, A. Zsögön, *Current Opinion in Plant Biology*. **60**, 102006 (2021).
5. A. Zsögön *et al.*, *Nature Biotechnology*. **36**, 1211–1216 (2018).
6. I. J. Wright *et al.*, *Nature*. **428**, 821–7 (2004).
7. T. J. Brodribb, T. S. Feild, G. J. Jordan, *Plant Physiology*. **144**, 1890–8 (2007).
8. L. Sack, N. M. Holbrook, *Annual Review of Plant Biology*. **57**, 361–381 (2006).
9. G. Haberlandt, *Jahrbücher für Wissenschaftliche Botanik*. **13**, 74–188 (1882).
10. R. B. Wylie, *American Journal of Botany*. **39**, 645–651 (1952).
11. I. Terashima, *Photosynthesis Research*. **31**, 195–212 (1992).
12. M. A. M. Barbosa *et al.*, *Plant, Cell & Environment*. **42**, 1575–1589 (2019).
13. T. Kenzo, T. Ichie, Y. Watanabe, T. Hiromi, *American Journal of Botany*. **94**, 764–775 (2007).
14. J. H. McClendon, *Plant Physiology*. **99**, 1677–1679 (1992).
15. A. Zsögön, A. C. Alves Negrini, L. E. P. Peres, H. T. Nguyen, M. C. Ball, *New Phytologist*. **205**, 618–626 (2015).
16. C. M. Jones, C. M. Rick, D. Adams, J. Jernstedt, R. T. Chetelat, *American Journal of Botany*. **94**, 935–947 (2007).
17. J. Lu *et al.*, *Hortic Res*. **8**, 1–14 (2021).
18. T. Lin *et al.*, *Nature Genetics*. **46**, 1220–1226 (2014).
19. A. V. Persikov *et al.*, *Nucleic Acids Research*. **43**, 1965–1984 (2015).
20. F. Baile, W. Merini, I. Hidalgo, M. Calonje, *The Plant Cell*. **33**, 2701–2715 (2021).
21. L. Truebestein, T. A. Leonard, *Bioessays*. **38**, 903 (2016).
22. D. Cui *et al.*, *PLoS Genet*. **9**, e1003759 (2013).
23. M. Gallei, C. Luschnig, J. Friml, *Current Opinion in Plant Biology*. **53**, 43–49 (2020).

24. J. Truskina *et al.*, *Nature*. **589**, 116–119 (2021).

25. M. Sagar *et al.*, *Plant Physiology*. **161**, 1362–74 (2013).

26. L. Sack, C. Scoffoni, *New Phytologist*. **198**, 983–1000 (2013).

27. S. A. M. McAdam *et al.*, *Plant physiology*. **175**, 351–360 (2017).

28. T. N. Buckley, L. Sack, M. E. Gilbert, *Plant Physiology*. **156**, 962–973 (2011).

29. K. Kawai, R. Miyoshi, N. Okada, *Trees*. **31**, 1–11 (2017).

30. M. A. Zwieniecki, T. J. Brodribb, N. M. Holbrook, *Plant Cell & Environment*. **30**, 910–921 (2007).

31. C. Aybar *et al.*, *Hydrological Sciences Journal*. **65**, 770–785 (2020).

32. D. Nikolopoulos, G. Liakopoulos, I. Drossopoulos, G. Karabourniotis, *Plant Physiology*. **129**, 235–243 (2002).

33. C. Bellasio, M. R. Lundgren, *New Phytologist*. **212**, 485–496 (2016).

34. A. Baresch, C. Crifò, C. K. Boyce, *New Phytologist*. **221**, 628–639 (2019).

35. J. Hu, A. Israeli, N. Ori, T. Sun, *The Plant Cell*. **30**, 1710–1728 (2018).

36. M. Arsic *et al.*, *Plant Physiology*. **183**, 1472–1483 (2020).

Acknowledgements

We thank Prof Alisdair Fernie and Prof Ralph Bock (Max-Planck Institute, Germany), Dr Federico Scossa (CREA, Italy), Prof José Jiménez-Gómez (INRA Versailles, France), Prof Andrew J. Thompson (Cranfield University, United Kingdom), Dr Karla Gasparini (University of São Paulo, Brazil) and Diego S. Reartes for valuable discussions and input on the manuscript. We also gratefully acknowledge the support and contributions of the UFV Plant Physiology Graduate Program.

Funding

Fundação de Amparo à Pesquisa do Estado de São Paulo (FAPESP), Brazil 2016/01128-9

Fundação de Amparo à Pesquisa do Estado de São Paulo (FAPESP), Brazil 2017/14953-0

Conselho Nacional de Desenvolvimento Científico e Tecnológico (CNPq).

Coordenação de Aperfeiçoamento de Pessoal de Nível Superior (CAPES), Brazil, Finance Code 001

Foundation for Research Assistance of the Minas Gerais State (FAPEMIG), Brazil RED-00053-16

Author contributions

Conceptualization: JEL, LEPP, MR, AZ

Methodology: LF, WCO, AF, LEPP, MR, AZ

Investigation: JDRM, BLR, BSL, JEL, LNS, TS

Funding acquisition: WCO, AF, LEPP, MR, AZ

Project administration: MR, AZ

Supervision: LF, WCO, AF, LEPP, MR, AZ

Writing – original draft: JDRM, AZ

Writing – review & editing: all authors

Data and materials availability

All data are available in the main text or the supplementary materials. No restrictions are placed on the materials, such as material transfer agreements.

Supplementary materials

Materials and Methods

Figs. S1 to S12

Tables S1 to S7

References

Supplementary Materials for

Auxin-driven ecophysiological diversification of leaves in domesticated tomato

Materials and Methods

Figs. S1 to S12

Tables S1 to S7

References

Materials and Methods

Plant material, growth conditions and breeding

Tomato seeds (*Solanum lycopersicum* cv Micro-Tom, MT and cv M82) were obtained from Prof Avram Levy (Weizmann Institute, Israel) and the Tomato Genetics Resource Center (TGRC, University of California, Davis), respectively. TGRC accession numbers: MT, LA3911; M82, LA3475. Seeds were sown on polyethylene trays containing Tropostrato® commercial substrate (São Paulo, Brazil) and grown in a greenhouse in Viçosa (642 m asl, 20º45´S; 42º51´W), with an average irradiance of ~800 µmol m^{-2} s^{-1}, photoperiod 12/12-h and air temperature 26/18°C day/night. Upon appearance of the first true leaf, seedlings of MT and M82 were transplanted to pots with a capacity of 350 mL and 3000 mL, respectively. Soil was fertilized with 2 g L^{-1} 10-10-10 NPK and 4 g L^{-1} limestone. For *in vitro* cultivation, seeds were sown in flasks containing 30 mL of half-strength MS medium (*36*) gellified with agar 4 g L^{-1}, pH 5.7 ± 0.05. The seedlings were kept under controlled conditions: photoperiod of 16-h/8-h day/night, light intensity of 45 ± 3 µmol m^{-2} s^{-1} and temperature of 25 ± 1 °C.

The tomato cv. M82 harbours the recessive *obv* mutant allele. To generate the tomato cv. M82 near-isogenic lines carrying the *OBV* functional allele from MT (M82-*OBV*), we performed the introgression of both the wild-type *OBV* allele and the OBV^{OE} transgene from either wild-type MT or MT plants harbouring the *obv* mutant allele and an OBV^{OE} transgene, respectively, following the scheme illustrated in fig. S14. Briefly, plants were grown in greenhouse under conditions described above. M82 and MT were crossed using the former as female parental and the latter as pollen donor. F_1 plants were self-pollinated, generating a segregating F_2 progeny. The F_2 seedlings resulting were screened for translucent veins and the bigger stature of M82. Selected plants were backcrossed (BC) with M82 parental, producing BC_1 F_2 seeds. This procedure of crossing and screening was carried until the BC_3 generation, where plants were manually self-pollinated and the progeny screened for homozygous plants (BC_3F_n).

GWAS analysis

The online repository of Solanaceae genetics and genomics information Sol Genomics Network (solgenomics.net) was used to access the database of 360 genomes of tomato cultivars and wild species (*16*). We focussed on a discrete region of chromosome 5 based

on the previously mapped location of *OBV* (*15*) and analysed genetic variations present in all 37 genes contained in the bin d-5E (Table S1). We then used the extensive database from the Tomato Genetics Resource Center, TGRC (tgrc.ucdavis.edu) to retrieve phenotypic data for different accessions of tomato cultivars and wild species and conduct the genotype × phenotype association.

The Genome-Wide Association Study (GWAS) was performed using data of 37 tomato accessions (25 wild-type and 12 mutants for *obv* phenotype, Table S2) and the Plink (v.1.07) software (*37*). A total of 3,218,302 single nucleotide polymorphisms (SNPs) with a minor allele frequency (MAF) greater than 5% were used for association analysis. The whole-genome significant cutoff was defined as P=1.554e-08 based on the Bonferroni correction method. A Manhattan plot was generated using the R package qqman (*38*). Gene annotation was obtained from International Tomato Annotation Group (ITAG, v.2.4) and visualized using the R package Gviz (*39*).

Structural modeling analysis

The analyses of functional domains in the OBV protein were done using the functional domain prediction tool from Interpro (www.ebi.ac.uk/interpro/), and the Logo plot was obtained by comparing of 324 protein sequences from the ortholog group of 39 plant species, using EVcouplings (evcouplings.org). The 3D model of the wild-type OBV protein was generated on SwissModel (swissmodel.expasy.org).

OBV homologs identification and phylogenetic inference

To identify *OBV* homologs in tomato and other plant species, we retrieved the ortholog group of proteins using the Plant Transcription Factor Database (planttfdb.gao-lab.org). We next aligned the sequences from the model species *A. thaliana* with MUSCLE (*40*). The alignment was submitted to trimAl (*41*) for alignment trimming and then submitted to FastTree (*42*) for tree inference. Trees were visually inspected using FigTree (tree.bio.ed.ac.uk/software/figtree/). Further phylogenetic inference using only *OBV* homologs were performed using MUSCLE, for sequence alignment, trimAl, for alignment trimming, SMS (*43*), for evolutionary model selection, and PHYML (*44*), for maximum likelihood tree inference. Final trees were annotated with taxonomic information from NCBI Taxonomy using TaxOnTree (bioinfo.icb.ufmg.br/taxontree).

The plant proteomes used in this work were retrieved from Sol Genomics Network, for tomato (ITAG v.4.0) (*45*), and from Uniprot (www.uniprot.org), for other species.

Molecular cloning

The coding sequence of *OBV* gene (1,149 pb) was reverse transcribed and amplified by PCR (Polymerase Chain Reaction) from RNA extracted from leaves of *Solanum lycopersicum* cv. Micro-Tom (wild-type) or the *obv* mutant, using the primers listed in Table S4. Young leaves (~2.0 cm) were collected for extraction of total RNA using Trizol® (Ambion, Life Technology), according to the manufacturer's recommendations. The cDNA synthesis was performed with SuperScript™ III First-Strand Synthesis System (Invitrogen). The amplicons were purified and cloned independently in the plasmids PCR8/GW/TOPO® (Invitrogen). Subsequently, each fragment was recombined in the overexpressing vector pK7WG2D,1 through Gateway® technology (*46*). The correct assembly of the construct was confirmed by PCR and Sanger sequencing.

For post-transcriptional gene silencing we used an interference RNA (RNAi) construct. A specific fragment of 223 pb (Appendix 1) from coding sequence of *OBV* gene was selected using BLAST queries against the Sol Genomics database (solgenomics.net/, ITAG release 2.40). The amplified fragment was purified and cloned into the plasmids PCR8/GW/TOPO® (Invitrogen), and then recombined in the gene silencing vector pK7GWiWG2 (I) (*46*). The assembly was confirmed by PCR and Sanger sequencing. The confirmed plasmids for overexpression or silencing were used to transform *Agrobacterium tumefaciens* (EHA105) by heat shock as previously described (*47*).

Plant transformation

A. tumefaciens EHA105 harbouring the plasmids described above was used to perform tomato plants transformation as described (*47*). Briefly, seeds were sterilized by agitation in 30% (v/v) commercial bleach (2.7% w/v sodium hypochlorite) for 15 min and rinsed with distilled water. 30 seeds of Micro-Tom or *obv* mutant were inoculated into flasks containing half-strength MS medium (*36*), vitamins B5, sucrose 30 g L^{-1} and agar 4 g L^{-1}. The pH of the medium was adjusted to 5.7 ± 0.05 and sterilized by autoclaving. The seeds were kept four days in the dark, 25 ± 1 °C, followed by four days under photoperiod of 16-h/8-h day/night and intensity 45 ± 3 μmol m^{-2} s^{-1}. The cotyledons of 8-days-old seedlings were sectioned and used in co-cultivation with *A. tumefaciens* in Root Inducing Medium (RIM) for 2 days, 25 ± 1 °C in the dark. Then, the explants were transferred to

Shoot Inducing Medium (SIM) and were kept in 25 ± 1 °C under photoperiod of 16-h/8-h and light intensity of 10-20 µmol m^{-2} s^{-1}, for four weeks. Explants were replated to fresh medium twice during this period. Well-developed shoots (≥ 5 cm) were transferred to flasks containing hormone-free MS medium, for shoot elongation and rooting. At all *in vitro* stages, the medium was supplemented with 300 mg L^{-1} timentin to suppress *A. tumefaciens* growth and 100 mg L^{-1} kanamycin for *in vitro* selection of transgenic plants.

Selection of overexpressing and silencing lines

Regenerated overexpressing and silencing T_0 plants were acclimatized under controlled conditions, photoperiod 16-h/8-h day/night, irradiance of 150 µmol m^{-2} s^{-1} and temperature of 25 ± 1 °C, using autoclaved Tropostrato® substrate and vermiculite (1:1) for four weeks. Subsequently, T_0 transgenic plants were transferred to greenhouse for genotyping and seed production.

To verify the transgene insertion, genomic DNA was extracted from young leaflets (*48*). First, the presence of the resistance gene *NEOMYCIN PHOSPHOTRANSFERASE II* (*neo*) was confirmed by PCR, for both constructs. A second confirmation was made to identify the transgene using a forward primer for *pCaMV 35S* and reverse specific for the construct of interest. The primers used are listed in Table S4.

To obtain homozygous plants, overexpressing and silencing lines were manually self-pollinated producing T_1, T_2, T_3 and T_4 seeds. Progeny tests were carried out on seeds derived from single plants through foliar spray of antibiotic (kanamycin 400 mg L^{-1} for five consecutive days). The plant populations (n=30) were 100% plants were antibiotic resistant (assessed visually as absence of leaf yellowing following kanamycin application) were considered homozygous. The assay was repeated on at least two subsequent generations.

Real-time quantitative PCR (RT-qPCR)

To assess the *Aux*/*IAA* transcriptional profile, leaf primordia (≤ 0.5 cm) were collected from Micro-Tom (wild-type), *obv* mutant and overexpressing lines. RNA was purified using ReliaPrep™ RNA Miniprep Systems (Promega), according to the manufacturer recommendations. The cDNA synthesis was performed with SuperScript™ III First-Strand Synthesis System (Invitrogen). Real-Time quantitative PCR reactions (qRT) were performed in a thermocycler Real-Time StepOnePlus PCR (Applied Biosystems) with a

final volume of 14 µL using reagent SYBR Green Master Mix (Thermo Fisher Scientific). The melting curves were analyzed for nonspecific amplifications and dimerization of primers. Absolute fluorescence data were analyzed using the software LinRegPCR (***46***) to obtain the values of quantification cycle (Cq) and calculate the primer efficiency. The abundance of transcripts was normalized against the geometric mean of two reference genes, *TIP4* and *EXPRESSED* (*49*). All the primers used are listed in Table S4.

To analyse the *OBV* expression profile in wild-type MT plants, the following tissues were collected: germinated seeds, root tips (≤ 2 cm), hypocotyls, leaf primordia (≤ 0.5 cm), expanding leaf 1 (≤ 2 cm), expanding leaf 2 (≤ 3 cm), mature leaf, flowers (petals + anthers), immature green fruits (IG3) and red ripe fruits (RR). RNA extraction and analyses was conducted as described above.

In situ hybridization

The *OBV* expression analyzed by *in situ* hybridization assay was performed as described previously (*50*). Apical meristems and leaf primordia of wild-type MT plants were collected and processed.

Phenotypic characterization

The morphological characterization was made in MT, *obv* mutant and overexpression lines in T_3 homozygous transgenic plants after anthesis. Plant height was measured from the soil level to the first inflorescence. The length and diameter of the internodes were obtained by measuring the fourth, fifth and sixth internodes counted from the bottom up. Stem diameter was measured from the cotyledons level using a mechanical pachymeter (Mitutoyo® Vernie Caliper model, Japan). Leaf number to the first inflorescence was obtained by counting of the leaves on main stem, from the bottom up. The leaf angle was determined based on the insertion of the fifth, sixth and seventh leaf, using a protractor. Biomass accumulation was obtained through root, stem and leaves dry mass by destructive analysis and oven-drying 60 days after germination. All measurements were conducted in at least 12 plants per genotype.

For leaf characterization, three terminal leaflets were selected per plant, in eight plants per genotype. The leaflets were digitized using an HP Scanjet G2410 scanner (Hewlett-Packard, Palo Alto, California, USA) Total leaf area was obtained digitizing all leaves and calculating the area in Image-Pro Plus. Specific leaf area (SLA) was calculated

through the ration between leaf area (LA) and leaf dry weight (LDW), as described by the equation: SLA (cm^2 g^{-1}) = LA/LDW.

Gas exchange, chlorophyll *a* fluorescence and *A*/*Cc* curves

Gas exchange analyses were performed in adult plants of cv. M82, M82-*OBV* (cv M82 harbouring the functional *OBV* allele) and M82-OBV^{OE} (M82 plants harbouring an *OBV* overexpression construct). All the evaluations described below were measured in fully expanded fifth leaf apical leaflets from base to apex. Gas exchange and chlorophyll *a* fluorescence parameters were determined simultaneously using an open-flow infrared gas analyzer (IRGA) system (model LI-6400XT, Li-Cor Inc., Lincoln, NE, EUA) equipped with an integrated fluorescence chamber of 2cm^2 (6400-40 Leaf Chamber, Li-Cor Inc.). The equipment was configured to provide a light intensity of 1000 µmol m^{-2} s^{-1}, CO_2 concentration of 400 µmol mol^{-1}, with the air flow in the chamber regulated to 300 µmol s^{-1}. For evaluation of dark respiratory activity (R_d), a 6 cm^2 leaf chamber with air flow set at 100 µmol s^{-1} was used. The effective quantum yield of photosystem II ($\phi PSII = (Fm' - Fs)/Fm'$) was determined by measuring the steady-state fluorescence (*Fs*) and the maximum fluorescence (*Fm'*), applying a saturating light pulse of 8000 µmol m^{-2} s^{-1} photons (*51*). Photochemical quenching ($qP = (Fm' - Fs)/(Fm' - F0')$) was calculated as described (*52*). The apparent rate of electron transport ($ETR = 0.5 \times 0.84 \times \phi PSII \times$ PAR) was calculated as described in ref. *53*, where 0.5 = fraction of the excitation energy distribution in the FSII; 0.84 = fraction of light absorbed by leaves; and PAR = photosynthetically active radiation.

The A/C_i response curves were measured under ambient O_2 and temperature, using PAR of 1000 µmol m^{-2} s^{-1} and injection of incremental CO_2 concentrations into the chamber (50, 100, 200, 300, 400, 500, 600, 700, 800, 900, 1000, 1200, 1400, 1600, 1800 µmol mol^{-1}). Calculations of chloroplast concentrations of CO_2 (C_c) and mesophyll conductance (g_m) were performed using the Harley method (*54*). The CO_2 compensation point quantified previously for tomato (*55*) was used as reference to calculate g_m and C_c. The maximum Rubisco carboxylation velocity (V_{cmax}), the maximum capacity for electron transport rate (J_{max}), and the use of phosphate trioses (TPU) were estimated based on C_i and C_c and normalized to 25°C (*56*). Stomatal, mesophyll and biochemical limitations were calculated as described (*57*). CO_2 and water vapor leaks were corrected according to the methodology described in ref. *58*.

Leaf hydraulic conductance (K_{leaf}^{max}) determinations

Leaf water potential (Ψ_{leaf}) was measured in the terminal leaflet of the fifth expanded leaf of MT, *obv* mutant and transgenic *OBV* overexpression lines, using a Scholander-type pressure chamber (model 1000, PMS Instruments, Albany, NY, USA). The leaf hydraulic conductance (K_{leaf}^{max}) was estimated using the transpiration rates and the water potential difference between the transpiring and non-transpiring leaflet. The non-transpiring leaflet consisted of the lateral leaflet of the same leaf, which was covered with plastic film in the night before the measurements. K_{leaf}^{max} was calculated according to equation:

$$K_{leaf}^{max} = E / (\Psi_L - \Psi_X)$$

Where E is the transpiration rate (mmol m^{-2} s^{-1}) determined during gas exchange measurements, and (Ψ_L – Ψ_X) corresponds to the pressure gradient between the transpiring and non-transpiring leaflet (MPa) (*8*). The parameters were determined in six plants per genotype.

K_{leaf}^{max} in the tomato cv. M82 background was determined in well-watered plants using the evaporative flow method (*57*) using a flowmeter. Healthy light-acclimated leaflets were cut underwater and immediately connected to the flowmeter. During connection with the equipment, the leaflet was maintained at an irradiance of 1000 µmol m^{-2} s^{-1} PPFD and at a constant airflow to maintain the transpiration rates (The leaf temperature varied between 26 and 32 ºC). After flow stabilization, the leaflets were removed from the system and placed in the dark (in plastic bags under high humidity to avoid dehydration) for 5 minutes to balance the water potential, this variable being quantified after that time. to calculate K_{leaf} the following equation was used:

$$K_{leaf}^{max} = F / \Psi_{leaflet}$$

where F is the steady-state leaf water flow. In this case, the K_{leaf} values were normalized using leaf area and water viscosity at 25 ºC.

Anatomical analyses

Expanded terminal leaflet from the fifth leaf were used for anatomical analyses. To obtain cross sections, a 1 × 0.5 cm fragment was excised from the leaf lamina and fixed in FAA70 (70% formalin-acetic acid-alcohol) for 24 h. Subsequently, the samples were dehydrated in an ethanol series (70%, 85% e 95%), under vacuum (-20 polHg). Pre-

infiltration was performed with resin and ethanol 95% (1:1) for 2 h under vacuum (-20 polHg), and infiltration was done in resin for one week. Cross-sections of 5 µm thickness were mounted on blades and stained with 0.05% toluidine blue. The images were analyzed under a light microscope (Zeiss AxioScope A1, Jena, Germany).

Vein density measurements

Vein density was measured in six terminal leaflets per genotype. The leaflets were collected and fixed in methanol 95% for 48 h, then the solution was changed to lactic acid 100% and incubated at 100°C until complete clarification (5-6 hours). The diaphanized leaflets were analyzed using a light microscope (Zeiss AxioScope A1, Jena Germany) and vein density was measured as length of veins per unit leaf area, using the software Image Pro-Plus® (imagej.nih.gov/ij/).

Histochemical GUS analysis

Seedlings of 20-days-old MT, *obv* mutant and overexpression lines were crossed to transgenic MT or *obv* lines carrying the auxin-responsive synthetic promoter (*DR5*) (*59*) fused to the reporter gene *UID* (encoding β glucoronidase). F_1 hybrid seeds were harvested and grown *in vitro* as described above. For each genotype, four three-week old seedlings were incubated in exogenous auxin (20 µM indole-3-acetic acid, IAA), or mock treated for 3 h. The seedlings were then incubated at 37 °C for 12 h in GUS staining solution (100 mM NaH_2PO_4, 10 mM EDTA, 0.1% Triton and 1 mM 5-bromo-4-chloro-3-indolyl-D-glucuronic acid; pH=7.2) to reveal GUS activity (*60*). After staining, the seedlings were washed in ethanolic series (70%, 80%, 95% e 100%), 1 h for each series at 37 °C to remove chlorophyll. Samples were then photographed using a using a light microscope (Zeiss AxioScope A1, Jena Germany).

Auxin quantification

The endogenous IAA levels were determined by gas chromatography-tandem mass spectrometry-selecting ion monitoring (Shimadzu model GCMS-QP2010 SE). First, the samples (50-100 mg fresh weight) were extracted and methylated (*61*). About 0.25 µg of the labeled standard [$^{13}C_6$] IAA (Cambridge Isotopes, UK) was added to each sample as an internal standard. The chromatograph was equipped with a fused-silica capillary column (30 m i.d., 0.25 mm, 0.5-µm-thick internal film) DB-5 MS stationary phase using

helium as the carrier gas at a flow rate of 4.5 mL min^{-1} in the following program: 2 min at 100°C, followed by a ramp of 10°C min^{-1} to 140°C, 25°C min^{-1} to 160°C, 35°C min^{-1} to 250°C, 20°C min^{-1} to 270°C and 30°C min^{-1} to 300°C. The injector temperature was 250°C, and the following mass spectrometer operating parameters were used: ionization voltage, 70 eV (electron impact ionization); ion source temperature, 230°C; and interface temperature, 260°C. Ions with mass-to-charge ratios of 130 and 189 (corresponding to endogenous IAA) and 136 and 195 (corresponding to [$^{13}C_6$]IAA) were monitored, and endogenous IAA concentrations were calculated based on extracted chromatograms at mass-to-charge ratios of 130 and 136.

Polar auxin transport assays (PAT)

Hypocotyl sections with 10-mm were excised from MT and *obv* seedlings 2-week-old and incubated in 5 mM phosphate buffer (pH 5.8) containing 1 µM IAA for 2 h at 25°C ± 2°C on a rotary shaker (200 rpm). The segments were placed between receiver blocks (1% [w/v] agar in water) and donor blocks (1% [w/v] agar in 5 mM phosphate buffer [pH 5.8] containing 1 µM IAA and 100 nM [^{3}H] IAA) oriented with their apical ends toward the donor blocks. After 4 h of incubation inside a humid chamber at 25°C ± 2°C, the receiver blocks were removed and stored in a 3 mL scintillation cocktail (Ultima Gold; PerkinElmer). Receiver blocks in the scintillation cocktail were shaken overnight at 100 rpm and 28°C ± 2°C before analysis in a scintillation counter. For the negative control, hypocotyl segments were sandwiched for 30 min between NPA-containing blocks (1% [w/v] agar in water containing 20 µM NPA) an auxin transport inhibitor. ^{3}H dpm was converted to fmol of auxin transported (*62*).

Auxin sensitivity assays

For hypocotyl elongation assays, MT and *obv* mutant seeds were grown on half-strength MS medium under photoperiod of 16-h/8-h day/night, 45 ± 3 µmol m^{-2} s^{-1} light intensity at 25 ± 1 °C. Hypocotyls from 8-days-old seedlings were excised in sections with 10-mm and preincubated in buffer (10 mM KCl; 1 mM MES-KOH [pH 6] and 1% [w/v] sucrose) for 2 h at 25°C in the dark to deplete endogenous auxin. Then, segments were incubated in the same buffer supplemented with α-naphthalene acetic acid (NAA) in increasing concentrations (0, 0.1, 1, 10, 100 e 1000 µM) for 24 h under agitation, light intensity of 45 ± 3 µmol m^{-2} s^{-1} at 25 ± 1 °C (*60*). For each genotype, three biological replicates were

conducted, each composed of 20 segments. Hypocotyls were photographed and the relative growth rate evaluated by Image Pro-Plus®.

For root regeneration from cotyledon explants, seeds of MT, *obv* mutant and overexpressing lines were germinated *in vitro* in half-strength MS medium under the conditions described above. Cotyledons from 12-days-old seedlings were excised and incubated in MS medium with or without IAA supplementation (0; 0.04; 0.4; 4 and 40 µM). The explants were kept in 25 ± 1 °C under photoperiod of 16-h/8-h and light intensity of 10-20 µmol m^{-2} s^{-1} for 15 days. The number of explants with visible roots was determined. Four replicates were conducted by genotype, each composed of 12 explants.

Statistical analysis

The experimental design was completely randomized. Data were submitted to analysis of variance (ANOVA) and the means were compared by Tukey test at 5% level of significance ($P \leq 0.05$).

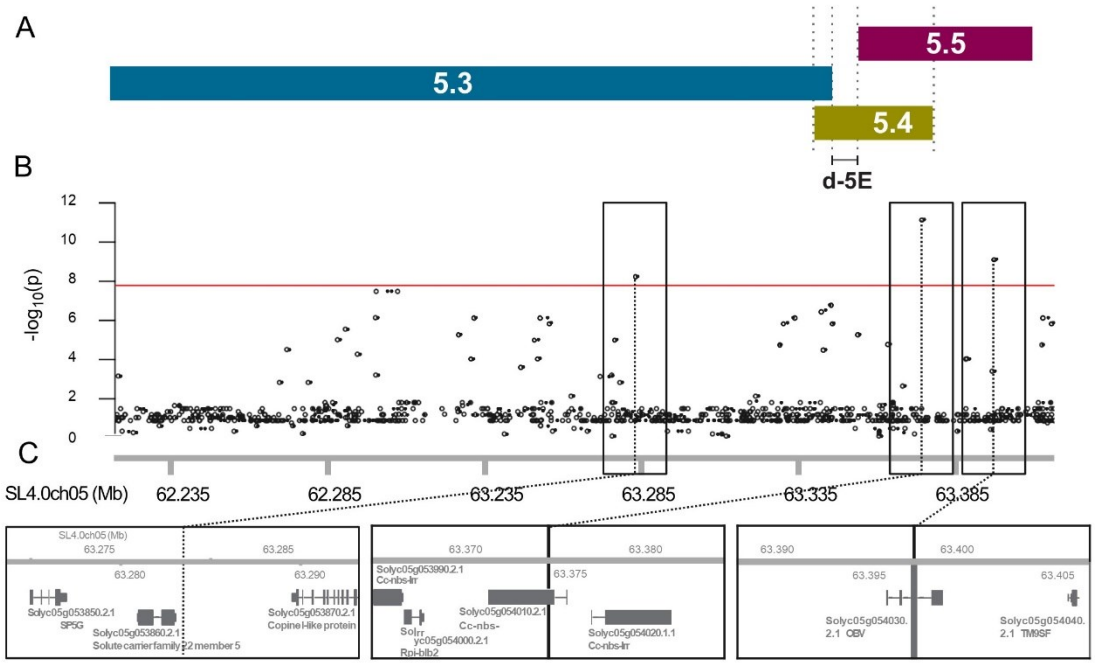

Figure S1. Mapping and identification of the *OBV* candidate gene.
(**A**) Schematic depiction of the *Solanum pennellii* segments of the introgression lines in tomato (redrawn from ref. *63*) showing the position of bin d-5E (*15*). (**B**) Manhattan plot of the GWAS for *obv* phenotype on d-5E region (63.73 to 64.03 Mb of chromosome 5). X-axis represents the chromosome position and the Y-axis represents the negative log10 of P-values per SNP derived from the association analysis. The red horizontal line represents the Bonferroni-corrected genome-wide significance threshold (P=1.554e-08). (**C**) Gene annotations surrounding SNPs with P-value below the significance threshold are shown in boxes.

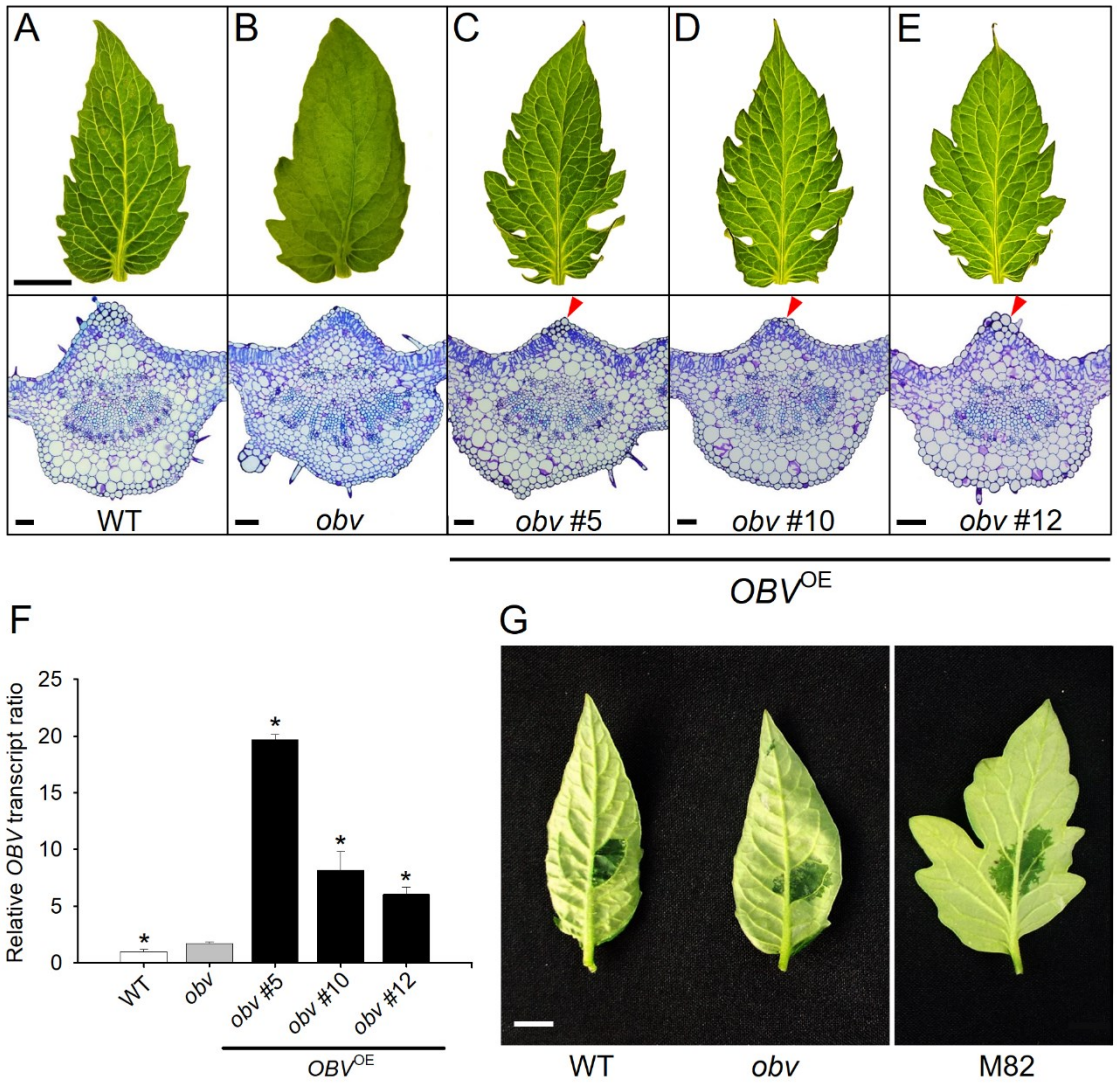

Figure S2. Complementation of the *obv* mutant with *OBV* functional allele.
(**A**-**E**) Representative leaflets and cross-sections of Micro-Tom (WT), *obv* mutant and *obv* complemented lines (OBV^{OE} #5, #10 and #12) T_1 generation. Red arrows show the recovery of BSEs in all OBV^{OE} lines. Bars = 1 cm and 100 µm for cross-sections. (**F**) Relative *OBV* mRNA levels in leaves of Micro-Tom (WT), *obv* mutant and three complemented lines (*obv*-OBV^{OE} #5, #10 and #12). Values were normalized against the MT (wild-type) sample. Asterisk show significant differences to the *obv* mutant. (**G**) In tomato (WT), BSEs divide the mesophyll into hermetic compartments, creating functionally heterobaric leaves. The compartmentalization of the mesophyll can be illustrated by a quick test, infiltrating water into the leaf blade. In heterobaric leaves, water distribution is limited by barriers imposed by BSEs. Whereas in leaves without the BSEs, homobaric, as in the *obv* mutant and in M82, the artificially infiltrated water spreads freely in the leaf.

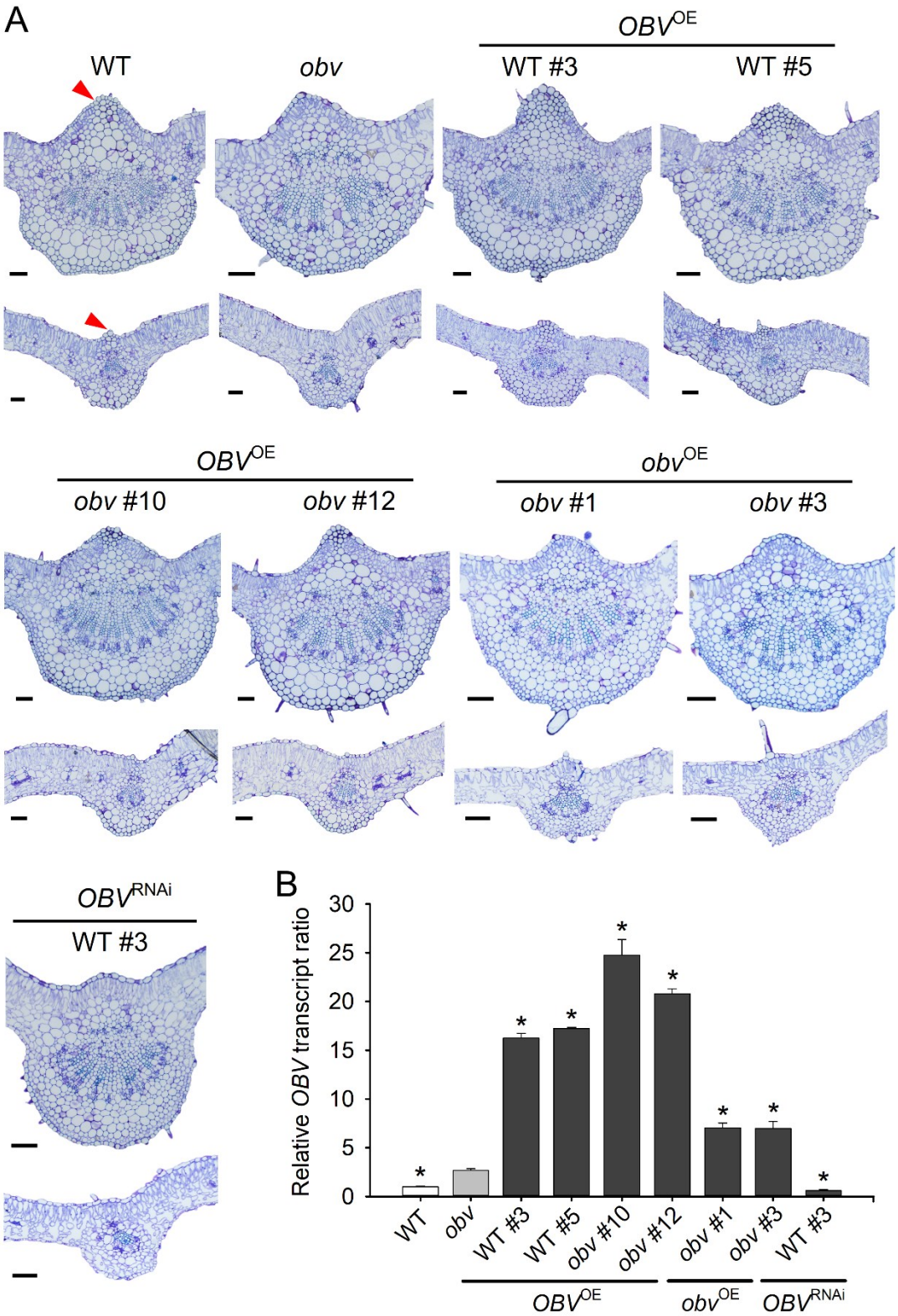

Figure S3. Complementation of the *obv* mutant and knockdown of *OBV* gene.

(**A**) Representative cross-sections of primary and secondary veins of Micro-Tom (WT), *obv* mutant, overexpressing lines with functional (OBV^{OE} #3, #5, #10 and #12) and mutant (obv^{OE} #1 and #3) allele, and knockdown line in WT background (OBV^{RNAi} #3). BSEs (red arrow) are present in all overexpressing lines with *OBV* functional allele, but not in overexpressing lines with *obv* mutant allele. In knockdown line, the

reduction in *OBV* expression resulted in complete elimination of BSEs in WT leaves. Bars = 100 µm. (**B**) Relative *OBV* mRNA levels in leaves of WT, *obv* mutant, overexpressing and RNAi lines. Values were normalized against the MT (wild-type) sample. Asterisk show significant differences to the *obv* mutant.

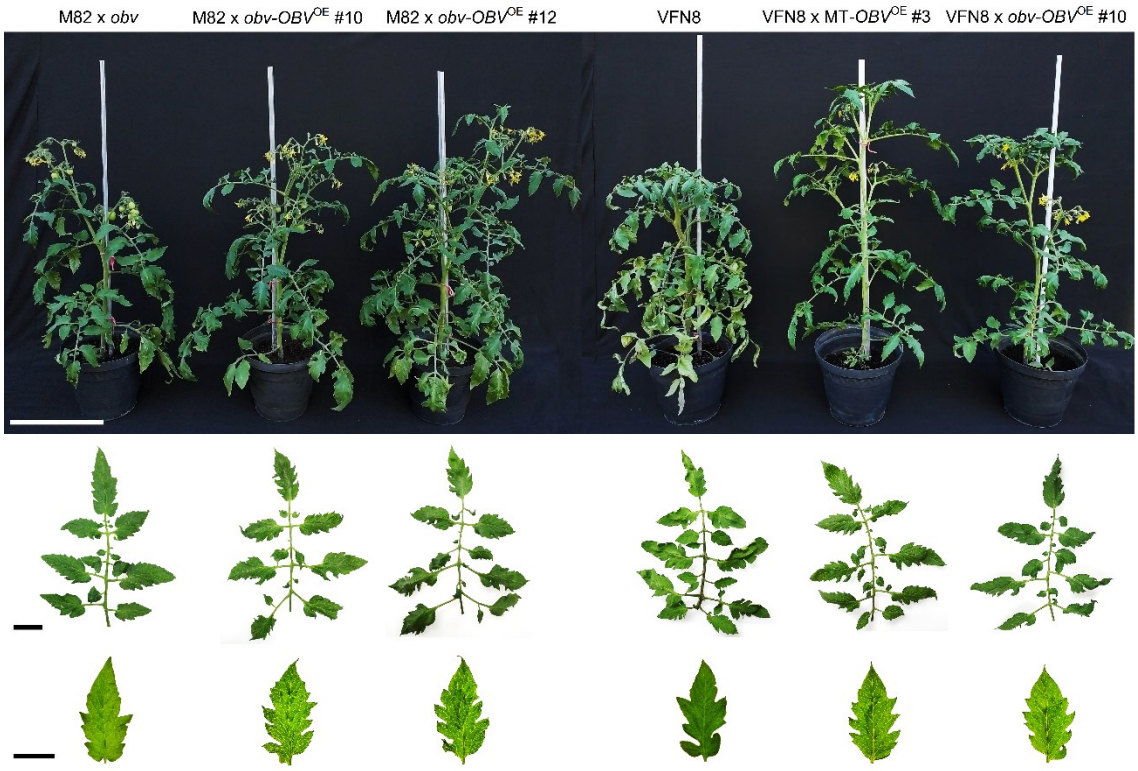

Figure S4. Morphology of M82, VFN8 and their respective hybrids with transgenic *OBV*-overexpressing (*OBV*^{OE}) plants in the Micro-Tom (MT) *obv* mutant genetic background. Representative F_1 generation plants from crossing of M82 × *obv*, M82 × *obv-OBV*^{OE} #10, M82 × *obv-OBV*^{OE} #12, VFN8, VFN8 × MT-*OBV*^{OE} #3 and VFN8 × *obv-OBV*^{OE} #10. Below are shown leaves and terminal leaflets. Cultivars M82 and VFN8 (both *obv* mutants) has dark veins and the complemented plants with *OBV*^{OE} allele recovered light veins phenotype. Plants were photographed 70 days after germination. Scale bars = 30 cm for plants; = 4 cm for leaves and leaflets.

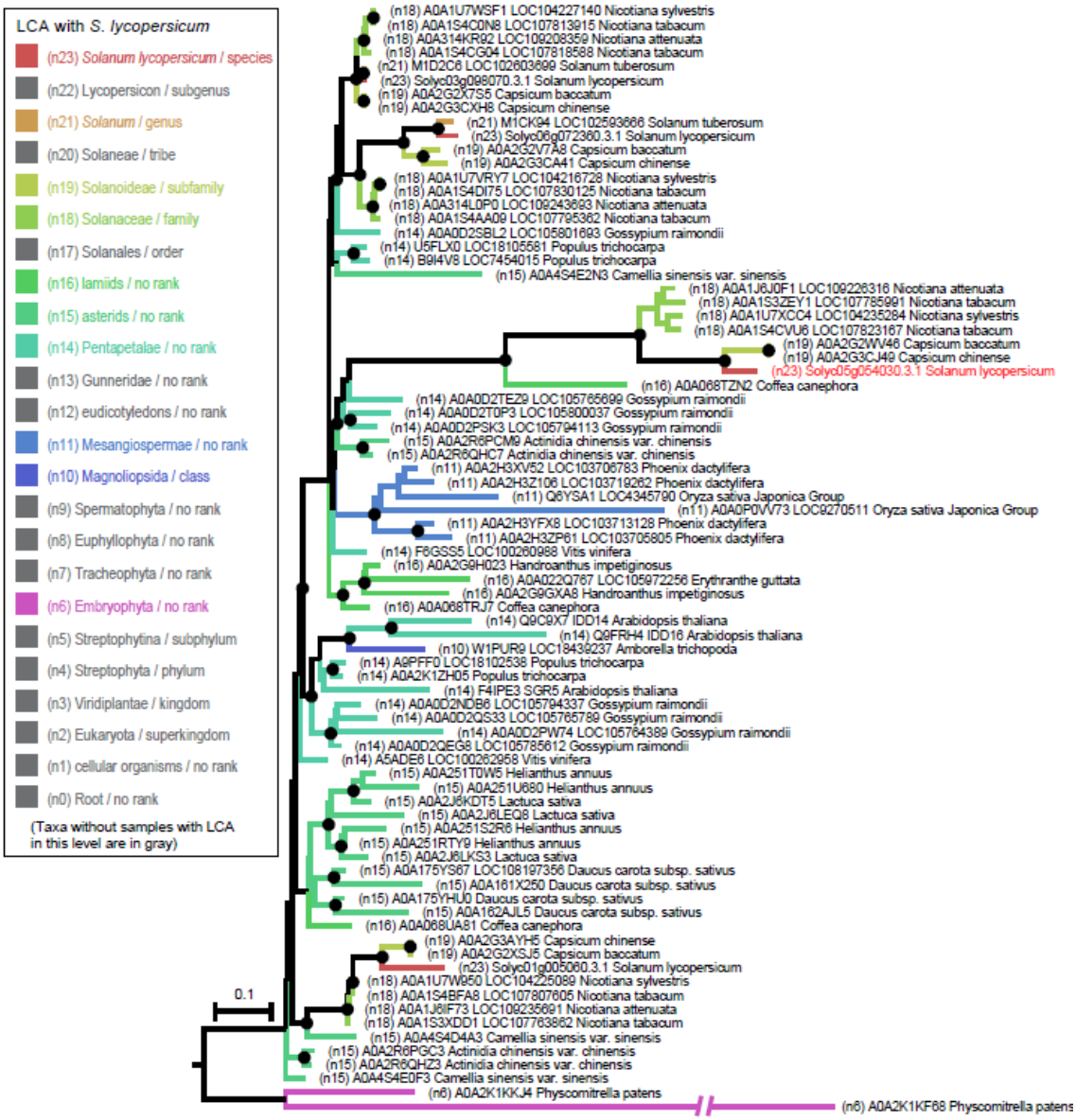

Figure S5. **Maximum likelihood tree of OBV family subclade comprising the tomato OBV (in red).** The tree was inferred with PHYML (substitution model: JTT+G+I, bootstrap replicates: 1000). Branches are colored according to the taxonomic relationship between the organism which a sample belongs to with *S. lycopersicum*, which were determined by consulting their Lowest Common Ancestor (LCA) in the NCBI Taxonomy tree. Leaf labels are comprised of (1) LCA level with *S. lycopersicum* (e.g. n11), (2) accession number; (3) gene name when exists and (4) species name.

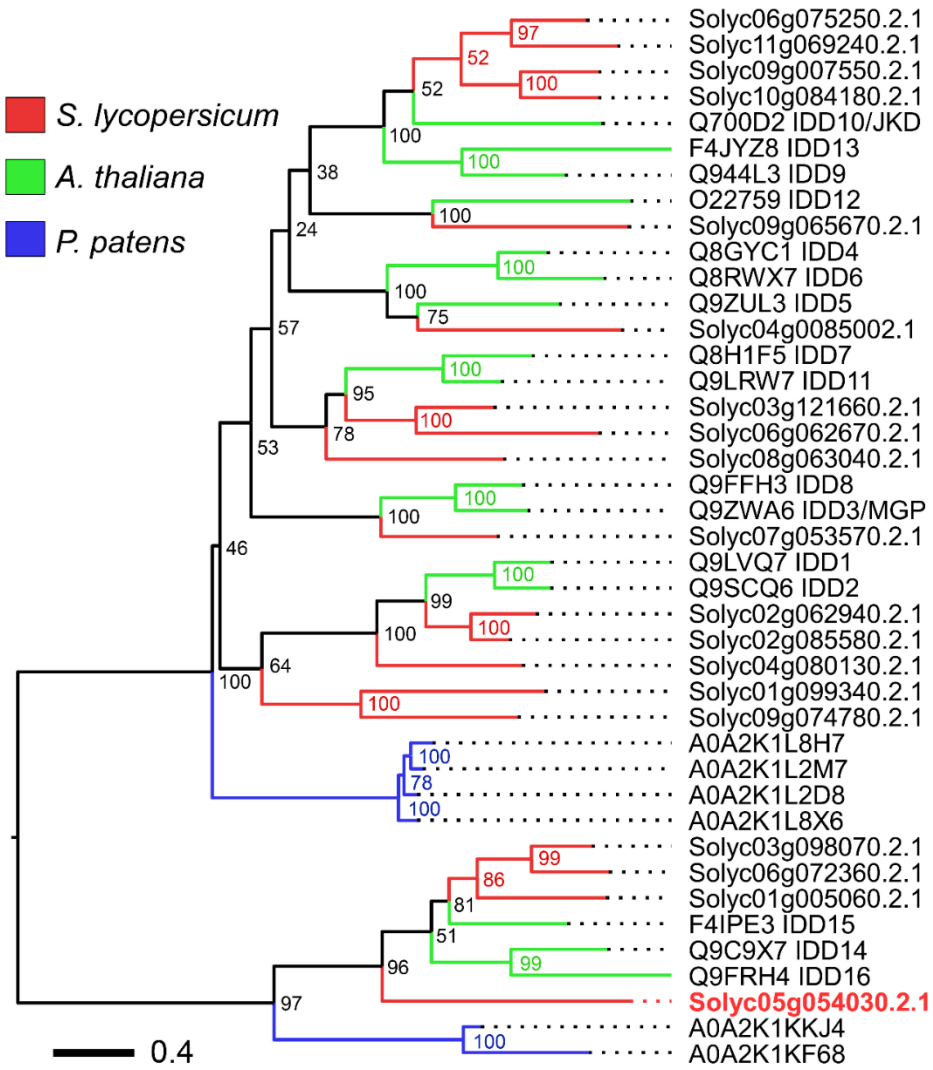

Figure S6. Phylogenetic reconstruction of OBV protein family.
Maximum likelihood tree of the OBV family from *S. lycopersicum*, subclade comprising the tomato OBV (in red) with its paralogs and orthologs in *Arabidopsis thaliana* and the basal angiosperm *Physcomitrella patens*, used as external group. The tree was inferred with PHYML (substitution model: JTT+G+I, bootstrap replicates: 1000).Branch support is shown on each node. Branches are colored according to the organism to which the protein sequence belongs to.

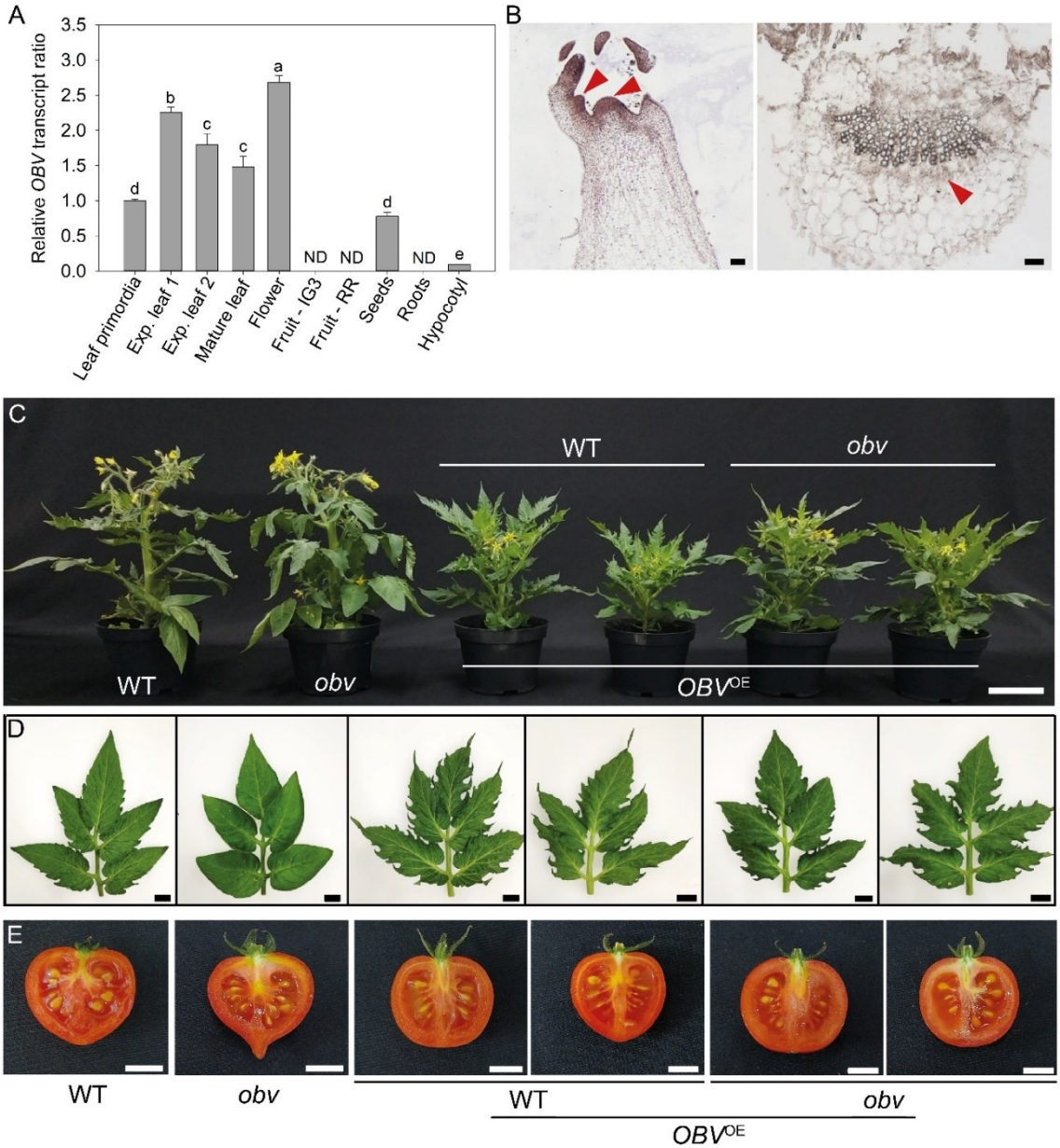

Figure S7. Expression patterns and pleiotropic effects of *OBV* in leaf insertion angle, leaf margin serration and fruit shape.

(**A**) Relative *OBV* mRNA levels in leaves (exp. = expanded), flowers, fruits (ripening stages represented by IG3 = immature green three; RR = red ripe), seeds, roots and hypocotyls of tomato cultivar Micro-Tom (MT). ND = not detected. (**B**) *In situ* hybridization showing *OBV* expression patterns in a longitudinal section of the shoot apex, including the apical meristem and leaf primordia and a cross-section of an expanded terminal leaflet. Arrowheads show the specific regions where *OBV* transcripts accumulate. Scale bars = 100 µm. Representative (**C**) plants, (**D**) fully expanded fifth leaf, and (**E**) mature fruits of MT, the *obv* mutant and homozygous T_3 transgenic lines overexpressing (OE) the *OBV* gene in either MT or *obv* mutant background. Scale bars = 10 cm (**C**) and 1 cm (**D**, **E**).

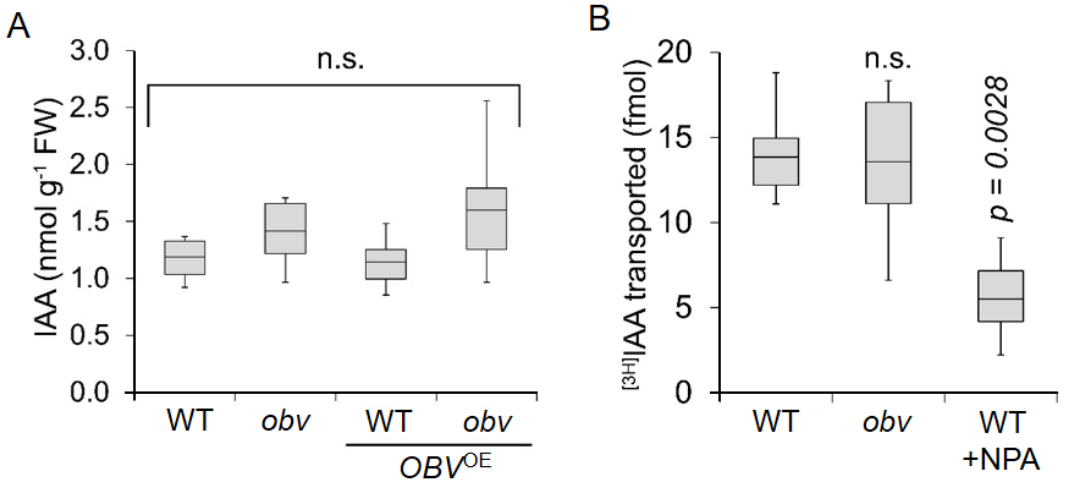

Figure S8. Influence of *OBV* on auxin concentration and transport.
(**A**) Auxin levels in leaf primordia (≤ 0.5 cm) of MT, *obv* mutant and *OBV*^{OE} lines, homozygous T_3. Data represent means of four biological replicates. Each biological replica was composed by a pool of three plants. Different letters indicate significant differences by Tukey's test at 5% probability. FW = Fresh weight. (**B**) [3H]IAA transport in detached hypocotyls of MT and *obv* mutant. The NPA is an auxin polar transport inhibitor and was used as negative control. Data are means (±SE) of at least ten biological replicates.

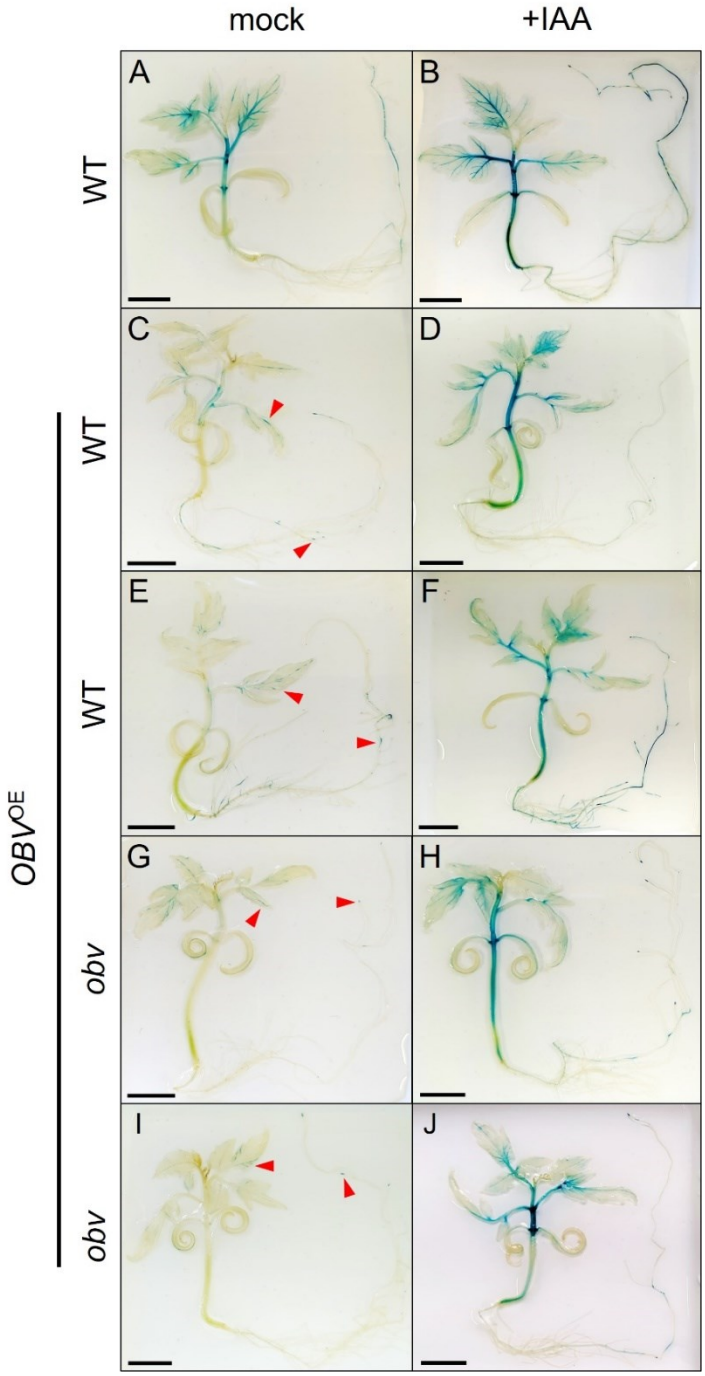

Figure S9. **Reduction of auxin sensitivity in *OBV* overexpressing lines.**
Histochemical GUS analysis in MT (MT x *DR5*::*GUS* F1) and overexpression lines (OBV^{OE} x *DR5*::*GUS* F1) seedlings at 30 days-old. (**A**, **C**, **E**, **G**, **I)** Expression pattern of *GUS* reporter gene fused to the auxin-inducible *DR5* promoter in wild-type seedlings and OBV^{OE} lines**.** **(B**, **D**, **F**, **H**, **J**) Expression pattern of GUS in MT and OBV^{OE} lines treated with exogenous auxin (20 µM IAA). Bars = 1 cm.

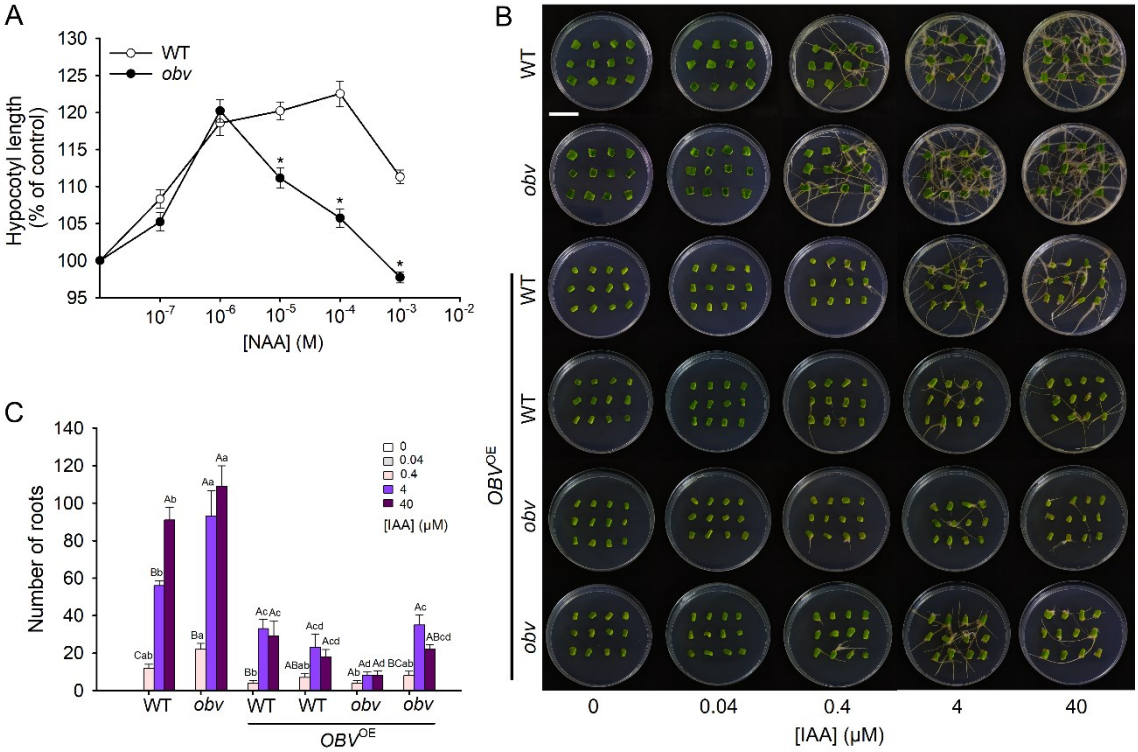

Figure S10. ***OBV* alters auxin sensitivity.**

(**A**) Auxin dose response in hypocotyl segments. Elongation is given as increase in percentage at final length over the initial length after 24 h incubation in a solution containing the NAA under increasing concentrations. Data are means (±SE) of three biological replicates with ≥ 20 segments for each replicate. Statistically significant differences compared with the MT were determined using Tukey's test: *P<0.05. (**B**) Auxin dose-response assay in 12-day-old cotyledon explants showing a significant reduction in the emission of roots in *OBV*^{OE} lines. (**C**) Total number of emitted roots induced from the concentration of 0.4, 4 and 40 µm IAA, after 15 days of cultivation. Different letters indicate statistically significant differences by Tukey's test, P < 0.05. Uppercase letters compare doses within the same genotype, lowercase letters compare dose effect between different genotypes. Bar = 1cm.

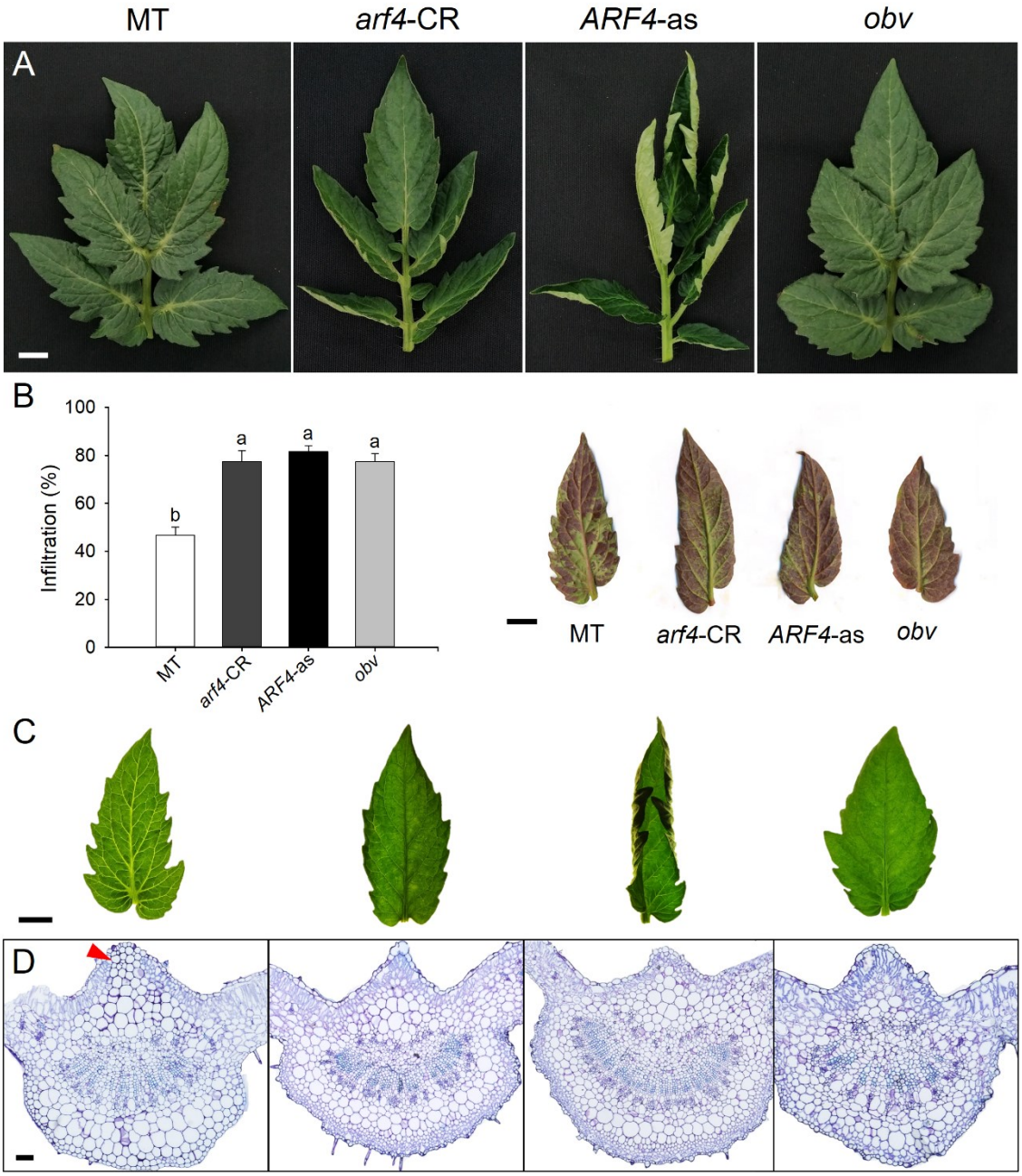

Figure S11. **Control of BSEs development by *ARF4* and *OBV*.**
(**A**) Representative leaf of MT, *arf4*-CR, *ARF4*-as, and *obv* mutant respectively. (**B**) Infiltration rate shows the percentage of leaf area filled with 1% acid fuchsin dye. The dispersion of the liquid in heterobaric leaves (MT) is hampered by compartmentalization of the mesophyll. In homobaric leaves (*arf4*-CR, *ARF4*-as and *obv*), the liquid is dispersed more easily due to absence of BSEs. The dye infiltration was made with same pressure in detached leaflets. Bars are mean values ± s.e.m. (n=7 leaflets). Different letters indicate significant differences by Tukey's test at 5% probability. (**C**) Details of terminal leaflet under transmitted light evidencing clear or dark vein phenotypes. (**D**) Leaf cross-sections at the midrib showing the presence (MT) and absence (*arf4*-CR, *ARF4*-as and *obv*) of BSEs. Bars = 1 cm and 100 µm for cross-sections.

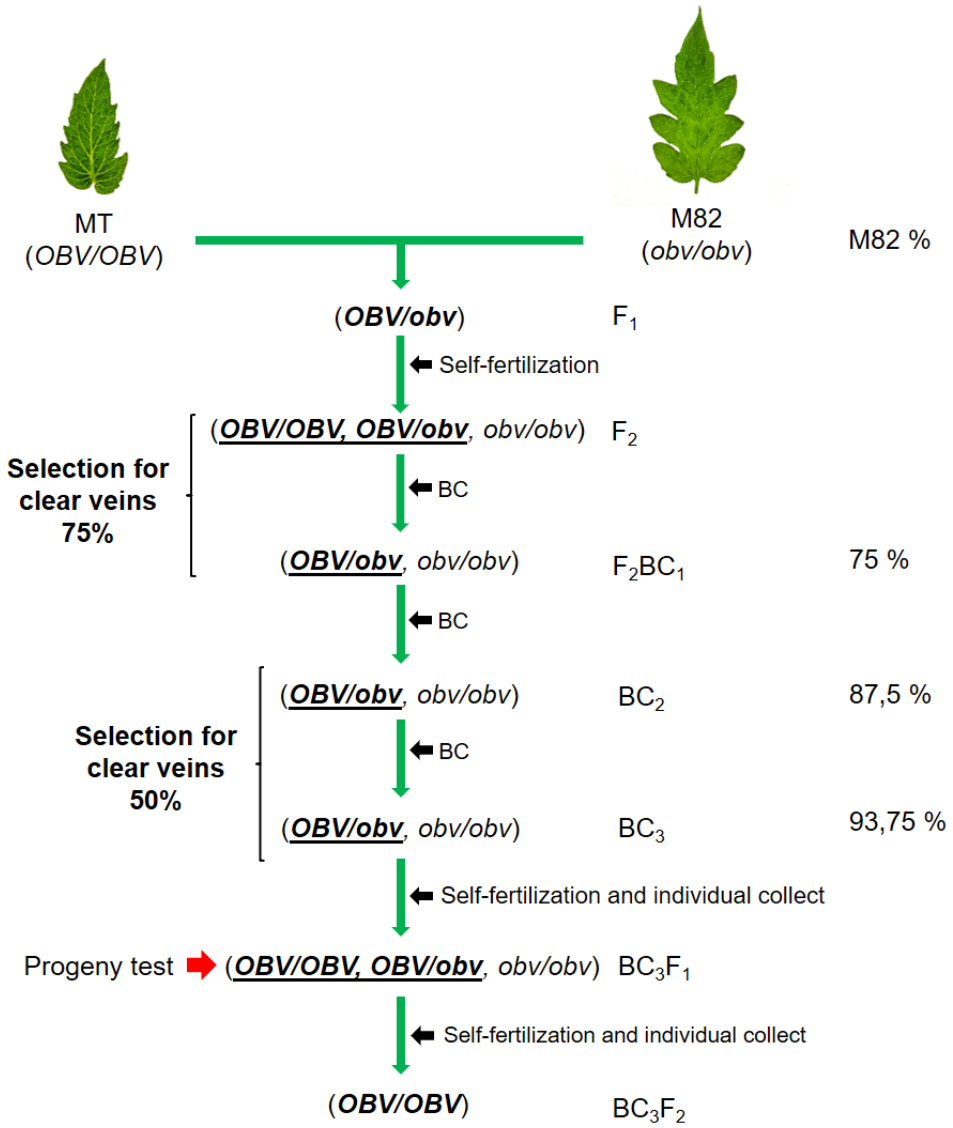

Figure S12. Pipeline for introgression of *OBV* functional allele into M82 background.
This pipeline shows the steps performed to obtain a near-isogenic line of M82 carrying *OBV* functional allele from MT (wild-type). The same steps were performed to obtain introgression lines with transgene (*obv-OBV*^{OE} generation T_4, homozygous). The selection of plants was made by choosing plants with clear veins and larger size. Progeny test was conducted at the end of introgression process and populations with 100% of individuals presenting clear veins were considered homozygous. BC = backcross.

Table S1. *OBV* candidate genes contained in bin d-5E of the *S. pennellii* introgression lines.

ITAG gene ID	Begin	End	Order	Annotation
Solyc05g053680.1.1	62878570	62882485	15862	Pectinesterase (AHRD V1 **** B9RWI7_RICCO); contains Interpro domain(s) IPR000070 Pectinesterase, catalytic
Solyc05g053690.1.1	62884728	62888637	15863	Ubiquitin carboxyl-terminal hydrolase (AHRD V1 **** B9GFW8_POPTR); contains Interpro domain(s) IPR001394 Peptidase C19, ubiquitin carboxyl-terminal hydrolase 2
Solyc05g053700.1.1	62890386	62893341	15864	Xyloglucan endotransglucosylase/hydrolase 1 (AHRD V1 **** D5HRN0_FRAAN); contains Interpro domain(s) IPR016455 Xyloglucan endotransglucosylase/hydrolase
Solyc05g053710.2.1	62894088	62900846	15865	TBC1 domain family member 13 (AHRD V1 ***- D3BTH5_POLPA); contains Interpro domain(s) IPR000195 RabGAP/TBC
Solyc05g053720.2.1	62901420	62908425	15866	Os12g0425600 protein (Fragment) (AHRD V1 **-- Q0INN2_ORYSJ); contains Interpro domain(s) IPR004348 Protein of unknown function DUF246, plant
Solyc05g053730.2.1	62909468	62913284	15867	Genomic DNA chromosome 5 TAC clone K21P3 (AHRD V1 *-*- Q9FJ19_ARATH)
Solyc05g053740.2.1	62913758	62915753	15868	Alkaline ceramidase (AHRD V1 ***- Q17KM2_AEDAE); contains Interpro domain(s) IPR008901 Alkaline phytoceramidase
Solyc05g053750.1.1	62920546	62926504	15869	Lipase (AHRD V1 **** Q1XBG1_RICCO); contains Interpro domain(s) IPR006693 AB-hydrolase associated lipase region
Solyc05g053760.2.1	62934657	62937298	15870	Chaperone protein dnaJ 20 (AHRD V1 ***- B6U349_MAIZE); contains Interpro domain(s) IPR001623 Heat shock protein DnaJ, N-terminal
Solyc05g053770.2.1	62942781	62950268	15871	At5g48610-like protein (Fragment) (AHRD V1 *-*- Q6XWA2_ARATH)
Solyc05g053780.2.1	62958028	62959831	15872	RNA binding protein-like protein (AHRD V1 ***- Q3HVL3_SOLTU); contains Interpro domain(s)

				IPR015465 RNA recognition motif, glycine rich protein
Solyc05g053790.1.1	62960914	62962215	15873	UDP-D-glucuronate 4-epimerase 4 (AHRD V1 **** D7LCH5_ARALY); contains Interpro domain(s) IPR016040 NAD(P)-binding domain
Solyc05g053800.2.1	62969281	62993468	15874	DNA repair protein Rad50 (AHRD V1 ***- A8IE27_TRITU); contains Interpro domain(s) IPR004584 Recombination/repair protein Rad50
Solyc05g053810.2.1	62993932	62998448	15875	Serine hydroxymethyltransferase (AHRD V1 **** D2D306_GOSHI); contains Interpro domain(s) IPR001085 Serine hydroxymethyltransferase
Solyc05g053820.2.1	63001106	63003424	15876	UDP-glucosyltransferase family 1 protein (AHRD V1 **** C6KI44_CITSI); contains Interpro domain(s) IPR002213 UDP-glucuronosyl/UDP-glucosyltransferase
Solyc05g053830.2.1	63004325	63011970	15877	Protein transport protein Sec23 (AHRD V1 ***- Q9LUG1_ARATH); contains Interpro domain(s) IPR006896 Sec23/Sec24 trunk region
Solyc05g053850.2.1	63036304	63038329	15878	SELF PRUNING 5G
Solyc05g053860.2.1	63042284	63044388	15879	Solute carrier family 22 member 5 (Predicted) (AHRD V1 ***- B3RF59_SORAR); contains Interpro domain(s) IPR016196 Major facilitator superfamily, general substrate transporter
Solyc05g053870.2.1	63050870	63056412	15880	Copine I-like protein (AHRD V1 ***- Q6YYC5_ORYSJ); contains Interpro domain(s) IPR010734 Copine
Solyc05g053880.2.1	63058550	63062825	15881	cDNA FLJ42396 fis clone ASTRO2001107 (AHRD V1 *-*- B3KW72_HUMAN)
Solyc05g053890.1.1	63063554	63065233	15882	Glucosyltransferase-like protein (AHRD V1 *-** Q9LXV0_ARATH); contains Interpro domain(s) IPR002213 UDP-glucuronosyl/UDP-glucosyltransferase
Solyc05g053900.2.1	63066251	63072361	15883	Aspartic proteinase nepenthesin-2 (AHRD V1 **-- B6TNP6_MAIZE); contains Interpro domain(s) IPR001461 Peptidase A1

Solyc05g053910.1.1	63083195	63084367	15884	Lipase family protein (AHRD V1 ***- Q2RAM0_ORYSJ); contains Interpro domain(s) IPR002921 Lipase, class 3
Solyc05g053920.1.1	63091393	63092700	15885	Lipase (Fragment) (AHRD V1 ***- Q9ZTW1_DIACA); contains Interpro domain(s) IPR002921 Lipase, class 3
Solyc05g053930.2.1	63100530	63103607	15886	ATP binding / serine-threonine kinase (AHRD V1 **** C5DB71_VITVI); contains Interpro domain(s) IPR002290 Serine/threonine protein kinase
Solyc05g053940.2.1	63104823	63109660	15887	Ras-related protein Rab-1A (AHRD V1 ***- B6RB23_HALDI); contains Interpro domain(s) IPR003579 Ras small GTPase, Rab type
Solyc05g053950.2.1	63111561	63115533	15888	Plasmid partition ParA protein (AHRD V1 ***- B8KJV3_9GAMM); contains Interpro domain(s) IPR010775 Protein of unknown function DUF1365
Solyc05g053960.2.1	63115904	63122815	15889	Cysteine-rich extensin-like protein-2 (AHRD V1 *-*- Q08195_TOBAC)
Solyc05g053970.2.1	63122564	63124254	15890	Amino acid transporter (AHRD V1 **** B9HY05_POPTR); contains Interpro domain(s) IPR013057 Amino acid transporter, transmembrane
Solyc05g053980.1.1	63124718	63125086	15891	NBS-LRR resistance protein-like protein (AHRD V1 ***- A1Y9Q9_SOLLC)
Solyc05g053990.2.1	63124981	63127903	15892	Cc-nbs-lrr, resistance protein
Solyc05g054000.2.1	63127954	63129059	15893	Late blight resistance protein Rpi-blb2 (AHRD V1 ***- Q38QB6_SOLBU)
Solyc05g054010.2.1	63132655	63137053	15894	Cc-nbs-lrr, resistance protein
Solyc05g054020.1.1	63138387	63142845	15895	Cc-nbs-lrr, resistance protein
Solyc05g054030.2.1	63157458	63160584	15896	C2H2L domain class transcription factor (AHRD V1 **-* D9ZIU3_MALDO); contains Interpro domain(s) IPR007087 Zinc finger, C2H2-type
Solyc05g054040.2.1	63167515	63172773	15897	Transmembrane 9 superfamily protein member 1 (AHRD V1 **** B6TZ24_MAIZE); contains Interpro domain(s) IPR004240 Nonaspanin (TM9SF)
Solyc05g054050.2.1	63173933	63177785	15898	Glutamate decarboxylase (AHRD V1 **** Q8LKR4_TOBAC); contains

Interpro domain(s)	IPR010107 Glutamate decarboxylase

Table S2. *OBV* allele in different *Solanum lycopersicum* accessions and wild species.

Accession ID	TGRC ID	Genotype	Leaf phenotype*	aa 135
RF_000	LA3435	Heinz 1706	Mutant (*obv*)	Arginine
TS-49_SNPs	LA3238	Earliana	Mutant (*obv*)	Arginine
TS-8_SNPs	LA4024	E-6203	Mutant (*obv*)	Arginine
TS-3_SNPs	LA3475	M82	Mutant (*obv*)	Arginine
TS-121_SNPs	LA3846	NC EBR-6	Mutant (*obv*)	Arginine
TS-60_SNPs	LA2009	New Yorker	Mutant (*obv*)	Arginine
TS-128_SNPs	LA0012	Pearson	Mutant (*obv*)	Arginine
TS-133_SNPs	LA3528	Peto 95-43	Mutant (*obv*)	Arginine
TS-186_SNPs	LA3214	Rowpac	Mutant (*obv*)	Arginine
TS-151_SNPs	LA2399	T-5	Mutant (*obv*)	Arginine
TS-171_SNPs	LA1706	UC-82	Mutant (*obv*)	Arginine
TS-1_SNPs	LA0490	VF36	Mutant (*obv*)	Arginine
--	LA1022	VFN8	Mutant (*obv*)	Arginine
RF_003	EA06086	Gardener's Delight	Wild-type (*OBV*)	Histidine
RF_001	LA2706	Moneymaker	Wild-type (*OBV*)	Histidine
RF_077	TR00018	Red Cherry	Wild-type (*OBV*)	Histidine
RF_055	LA1401	*S. galapagense*	Wild-type (*OBV*)	Histidine
RF_074	LA0716	*S. pennellii*	Wild-type (*OBV*)	Histidine
RF_047	LA1578	*S. pimpinellifolium*	Wild-type (*OBV*)	Histidine
TS-195_SNPs	LA0516	Ace	Wild-type (*OBV*)	Histidine
TS-9_SNPs	LA2838A	Ailsa Craig	Wild-type (*OBV*)	Histidine
TS-155_SNPs	LA0533	Condine Red	Wild-type (*OBV*)	Histidine
TS-278_SNPs	LA0517	Early Santa Clara	Wild-type (*OBV*)	Histidine
TS-5_SNPs	LA2711	Edkawi	Wild-type (*OBV*)	Histidine
TS-212_SNPs	LA3242	Flora-Dade	Wild-type (*OBV*)	Histidine
TS-4_SNPs	LA3856	Hawaii 7998	Wild-type (*OBV*)	Histidine
TS-200_SNPs	LA3320	Hotset	Wild-type (*OBV*)	Histidine
TS-264_SNPs	LA0025	King Humbert 1	Wild-type (*OBV*)	Histidine
TS-10_SNPs	LA0502	Marglobe	Wild-type (*OBV*)	Histidine

TS-163_SNPs	LA1504	Marmande	Wild-type (*OBV*)	Histidine
TS-239_SNPs	LA3845	NC EBR-5	Wild-type (*OBV*)	Histidine
TS-237_SNPs	LA3243	Platense	Wild-type (*OBV*)	Histidine
TS-206_SNPs	LA0089	Prince Borghese	Wild-type (*OBV*)	Histidine
TS-122_SNPs	LA1090	Rutgers	Wild-type (*OBV*)	Histidine
TS-6_SNPs	LA3008	San Marzano	Wild-type (*OBV*)	Histidine
TS-152_SNPs	LA1021	Santa Cruz B	Wild-type (*OBV*)	Histidine
TS-188_SNPs	LA1506	Stone	Wild-type (*OBV*)	Histidine
TS-97_SNPs	LA0154	Tiny Tim	Wild-type (*OBV*)	Histidine
--	LA3911	MT (Micro-Tom)	Wild-type (*OBV*)	Histidine

Table S3. GO Enrichment Analysis by Gene Ontology for the *OBV* gene. Source: **http://www.geneontology.org/page/go-enrichment-analysis**

GO-group	GO-ID	Term
Biological process	GO:0009965	leaf morphogenesis
	GO:0048573	photoperiodism, flowering
	GO:0010363	regulation of plant-type hypersensitive response
	GO:0009937	regulation of gibberellic acid mediated signaling pathway
	GO:0048765	root hair cell differentiation
	GO:0009959	negative gravitropism
	GO:0031348	negative regulation of defense response
	GO:0045604	regulation of epidermal cell differentiation
	GO:0010075	regulation of meristem growth
	GO:0010029	regulation of seed germination
	GO:0010260	organ senescence
	GO:0009867	jasmonic acid mediated signaling pathway
	GO:0048527	lateral root development
	GO:0009590	detection of gravity
	GO:0006612	protein targeting to membrane
	GO:0010167	response to nitrate
	GO:0016558	protein import into peroxisome matrix
	GO:0010310	regulation of hydrogen peroxide metabolic process

	GO:0010431	seed maturation
	GO:2000904	regulation of starch metabolic process
	GO:0048510	regulation of transition from vegetative to reproductive phase
	GO:0009862	salicylic acid mediated signaling pathway
	GO:0051302	regulation of cell division
	GO:0010031	circumnutation
	GO:0010106	cellular response to iron ion starvation
	GO:0045893	positive regulation of transcription, DNA-templated
	GO:0035304	regulation of protein dephosphorylation
	GO:0009958	positive gravitropism
	GO:0000165	MAPK cascade
	GO:0015706	nitrate transport
	GO:0006635	fatty acid beta-oxidation
	GO:0006826	iron ion transport
	GO:0009617	response to bacterium
	GO:0045449	regulation of transcription, DNA-templated
Cellular component	GO:0005634	nucleus
	GO:0005667	transcription factor complex
Molecular function	GO:0003700	sequence-specific DNA binding transcription factor activity
	GO:0042803	protein homodimerization activity
	GO:0044212	transcription regulatory region DNA binding
	GO:0043621	protein self-association
	GO:0008270	zinc ion binding
	GO:0046982	protein heterodimerization activity

Table S4 Sequences used for phylogenetic and alignment analysis.

See Supplemental Excel Spreadsheet

Table S5. Oligonucleotides DNA sequence for PCR primers and RNAi target sequence used in this study. The sequence of oligonucleotides used for cloning, genotyping and RT-qPCR are listed.

Target gene	Forward sequence (5'-3')	Reverse sequence (5'-3')	Purpose
OBV	CACCCAATATTTCATCATATTGAATATA TCTC	GATTTTTTATATGAGTGAACAATG	cloning/ genotyping
M13	GTAAAACGACGGCCAG	CAGGAAACAGCTATGAC	cloning
35S p	CCTCGGATTCCATTGCCCA	----	genotyping
NPTII	GAGGCTATTCGGCTATGACTGG	ATCGGGAGCGGCGATACCGTA	genotyping
OBV	ACTTGTGGTACTAGAGGCCATTCT	CATGTGGTGGGATATGAGTTGTAGT	qPCR
TIP4	GCTGCGTTTCTGGCTTAGG	ATGGAGTTTTTGAGTCTTCTGC	qPCR
EXP	GCTAAGAACGCTGGACCTAATG	TGGGTGTGCCTTTCTGAATG	qPCR
ARF1	TGCTTTAGGAATGTGGAAGTC	GGAACCATTCTCACCATAACC	qPCR
ARF2A	GCAAGGTCAAGAGTTATCGA	CATTGGTTTCTCAGACAAGTC	qPCR
ARF2B	CTGGGTTAAGCGACAAGCTC	CCCCGCATTTGATACAGAG	qPCR
ARF3	GATTGTTTTGCTCCCTTGGA	GTGGCTGACCCCGATAGATA	qPCR
ARF4	TGAAAGCCATCAACTCTCGG	ATCCCATCTGACCATCAAGCATC	qPCR
ARF5	TTCCGAGCCAAGAAAAGAAA	CACTCGCATCAGTTGGAAGA	qPCR
ARF6A	CCAACATATCCCTAGTACTTCAG	GTGCCTGAGATATTAGTTGGT	qPCR
ARF6B	AGCCCATCAGAGTTTGTCATAC	ATTGTGCCCATATACCTACGAA	qPCR
ARF7A	CGCCTCTGGATTACTCAATG	CACCCTGTCGTTAGCAAATG	qPCR
ARF7B	TTCGCATGATGTTTGAGACT	CTTGGAACTGAAGAATGGACTA	qPCR
ARF8A	AGCCCGTCCAATATGTTCAG	TTTGATGGTTGCTTCTGCTG	qPCR
ARF8B	CATCTCCTTCCGACCACAGT	TGGTGGATCAATTTGTCCTGC	qPCR
ARF9A	CAAAGAGTTCCATCATTCAATCTC	GACCTCATCATTGTCTTCTTCAG	qPCR
ARF9B	AGGTCCATTAGTTGATGTTCCA	CTTGTTCAGCCAGAAGTTGAA	qPCR
ARF10A	ATTCTCTGTGCCTAGATACTG	CTATAAATGTGCCTAAACTTCCA	qPCR
ARF10B	GACATGGGATGAACCAGATTTG	GGAAACTCTTGTGGCAAACAC	qPCR
ARF16A	CGGTATTGACAACTCGGAGAT	TTCGCGCTGTTTTCATGAAG	qPCR
ARF16B	TACCATGATTCCCAAGCCAAGTA	GACCAAACAGTACGAATTGTGT	qPCR
ARF17	GCATCCGATTAGTCAGAGTGAAG	CCTCCTCCATTATTCGCATCTG	qPCR
ARF18	AAGCTTCCTATCTTATCATTGGA	AATCTACACTCGGCATTGTC	qPCR
ARF19	CTGGTGGATGAATCTGTTGTC	TACTTAGACAGCTCTGAACCT	qPCR
ARF24	CTGGTTCATTGTTGGATGTTTC	CCACATGAAGTCTTGGAAAGTAG	qPCR
IAA1	TGTTGCCAAGGCACAAATTG	GGTTGGATGATGTTTTTCCTGTTAG	qPCR
IAA2	ACAGTTCCATCATCCACAAG	ACCATCCATGCTCACTTTAAC	qPCR
IAA3	GCCACCAGTTCGATCATACA	ATAAGGTGCTCCATCCATGC	qPCR
IAA4	ACTCCACCTGTTGCCAAGAC	AGATAAGGGGCTCCATCCAT	qPCR
IAA7	TGATTCATGCAAGCGTTTACG	TGGCTCTTGGTGCTAGTCCAA	qPCR
IAA8	AAGGATCTATCTTCAGCACTAGA	TCCGCCAATTTGCTTTCTTTA	qPCR
IAA9	CAGAGGGGAAGTTTCTGTCG	CAACCTGTGCCTTTGTAGCA	qPCR

IAA11	GATGAAACTGGGCTTGAATTG	CACAACCTGACTGGCACTTG	qPCR
IAA12	ACAAAGATGGAGACTGGATGCT	CGGTCTTCCACCATTTCTTCC	qPCR
IAA13	AAGCGGTGAAAAGGAACAAG	TGCTTCTGAGGGATTCTTGGA	qPCR
IAA14	CCACCAGTGAGATCATTTAGGA	AGGTGCACCATCCATGCAAA	qPCR
IAA15	ATCGGAGACAGCCAAATCAG	TTTGCTGGAGGTTTGTTTCC	qPCR
IAA16	GTGCCAAGCTCTAATGATCCT	GCACCGTCAACACTAACTT	qPCR
IAA17	CAAGAATTATTTGATGCCTTAACCA	CTATTCAAAAGGTCCATCAGTTTCC	qPCR
IAA19	TGTCGGCGATGTTCCATG	GTCTCTTGCTCCAAGCCCTAT	qPCR
IAA21	TGTTCAAGCTCAACATAGGTGAAT	CCAACAAGCATCAAATCACCTT	qPCR
IAA22	CTGAGCTGAGATTAGGGTTACC	AGGAGCTGTCCATCTCTGAT	qPCR
IAA23	CACTCAACTCCTTAAAGCAATGGA	TCCTCAGTCTCTTGCATGATGAC	qPCR
IAA26	CCTCCAATTCGTTCCTTTAGGA	GGAATACCATCCATGTTGATCTT	qPCR
IAA27	GCAAGAGAAGCTCAGTGA	ACATCTCCCAAGGAACATCG	qPCR
IAA29	GGTTTTGATGATAGCTTCTCCGAT	CGTCTTACGTTCAACTACTCCTT	qPCR
IAA32	AGGAATGACCAATGGAGGATT	GGGAAGAATGCTTCATCTTTCC	qPCR
IAA33	CCTTGTTGGTGATCTCAGTTG	CTTCCAGTGCGTGAATTTGG	qPCR
IAA35	AAATGGAAGGAGTTGGAATTGC	ATGGTACATCACCAGCAAGAAG	qPCR
IAA36	TGGAAGGAGTAGCCATTGGA	TGGTACATCTCCAGCAAGCA	qPCR

OBV Sequence selected for the post-transcriptional gene silencing by interference RNA (RNAi)

GTACTCCAGATCCCGATGCACAAGTTGTATATCTTACAGCTGAGATGTTAATGGAATCTGATCGTTACGTT
TGTGAAATCTGCAACCTTAGCTTTCAAAGAGAGCAAAATCTACAAATGCATCGTCGTCGCCATAAGGTTCC
ATGGAAGTTGAAGAAGAAGGAAGAAGAGAAAAATGAGATGGATCAAGTTATTAAGAAGAGAGTATATGT
GTGTCCAGAGCC

Table S6. Growth parameters measured in Micro-Tom (MT), *obv* mutant and overexpressing lines. Measurements were performed at 50 days after germination. Data are means ± se (n = 12 plants). Different letters indicate statistically significant differences (Tukey's test, P < 0.05).

			MT		*obv*	
Parameters	**MT**	***obv***	***OBV*^{OE} #3**	***OBV*^{OE} #5**	***OBV*^{OE} #10**	***OBV*^{OE} #12**
Plant height (cm)	15.89 ± 0.43a	15.30 ± 0.30a	10.32 ± 0.20b	8.43 ± 0.19c	10.99 ± 0.27b	10.04 ± 0.20b
Internode length (4th)	1.30 ± 0.07a	1.19 ± 0.05a	0.77 ± 0.05b	0.52 ± 0.02c	0.81 ± 0.05b	0.70 ± 0.03bc
Internode length (5th)	1.52 ± 0.05a	1.57 ± 0.09a	0.97 ± 0.04b	0.70 ± 0.03c	1.01 ± 0.05b	0.88 ± 0.03bc
Internode length (6th)	1.52 ± 0.09a	1.59 ± 0.08a	1.03 ± 0.04b	0.77 ± 0.03c	1.08 ± 0.04b	1.04 ± 0.04b
Internode diameter (4th)	0.64 ± 0.02b	0.70 ± 0.01a	0.60 ± 0.01b	0.47 ± 0.01c	0.66 ± 0.02ab	0.63 ± 0.01b
Internode diameter (5th)	0.68 ± 0.02ab	0.74 ± 0.01a	0.62 ± 0.01b	0.48 ± 0.01c	0.66 ± 0.02b	0.64 ± 0.01b
Internode diameter (6th)	0.72 ± 0.02a	0.73 ± 0.01a	0.63 ± 0.01b	0.49 ± 0.01c	0.64 ± 0.02b	0.61 ± 0.01b
Stem diameter (cm)	0.57 ± 0.01ab	0.58 ± 0.02a	0.51 ± 0.01b	0.43 ± 0.01c	0.55 ± 0.02ab	0.54 ± 0.02ab
Leaves to 1st inflorescence	11 ± 0.18a	10 ± 0.15b	11 ± 0.13a	11 ± 0.12a	11 ± 0.23a	11 ± 0.19a
Leaf angle (5th)	72 ± 2.24a	63 ± 2.47b	63 ± 1.26b	57 ± 1.04b	61 ± 1.38b	57 ± 1.72b
Leaf angle (6th)	75 ± 2.22a	64 ± 2.62b	46 ± 1.82c	45 ± 1.87c	48 ± 1.98c	45 ± 1.09c
Leaf angle (7th)	72 ± 2.78a	59 ± 2.94b	43 ± 1.37c	39 ± 0.97c	42 ± 1.72c	42 ± 1.25c
Leaflets number (5th)	5 ± 0.0a	5 ± 0.11a	5 ± 0.18a	5 ± 0.19a	5 ± 0.0a	5 ± 0.0a
Leaflets number (6th)	6 ± 0.22a	6 ± 0.23a	6 ± 0.19a	7 ± 0.29a	7 ± 0.26a	7 ± 0.34a
Leaflets number (7th)	7 ± 0.40a	7 ± 0.41a	7 ± 0.29a	8 ± 0.25a	8 ± 0.24a	8 ± 0.30a
Perimeter/area (cm^{-1})	1.65 ± 0.08c	1.23 ± 0.03c	2.63 ± 0.15ab	2.93 ± 0.10a	2.26 ± 0.09b	2.66 ± 0.13ab
Perimeter^2/area	34.97 ± 2.38cd	24.01 ± 0.81d	58.29 ± 4.53ab	66.60 ± 3.95a	47.31 ± 3.03bc	68.17 ± 4.70a
Leaflets area (cm^2)	13.50 ± 0.83b	16.32 ± 0.97a	8.76 ± 0.49c	7.65 ± 0.25c	9.38 ± 0.43c	9.79 ± 0.39c
Total leaf area (cm^2)	339.2 ± 24.8a	365.4 ± 19.1a	321.5 ± 14.0a	279.4 ± 12.2a	361.8 ± 24.8a	356.9 ± 29.3a
Circularity	0.39 ± 0.02b	0.53 ± 0.01a	0.25 ± 0.02cd	0.21 ± 0.01cd	0.29 ± 0.02c	0.20 ± 0.01d
Serration number	11.52 ± 0.49b	8.28 ± 0.34c	13.57 ± 0.38a	14.90 ± 0.36a	13.28 ± 0.52ab	13.90 ± 0.55a
SLA (cm^2g^{-1})	312.3 ± 5.40	341.2 ± 12.37	366.6 ± 5.92	408.4 ± 7.69	389.8 ± 2.75	375.8 ± 5.41

Root dry weight (g)	0.35 ± 0.03ab	0.36 ± 0.01a	0.19 ± 0.01cd	0.11 ± 0.001d	0.26 ± 0.03bc	0.23 ± 0.01c
Stem dry weight (g)	1.33 ± 0.12a	1.57 ± 0.08a	0.67 ± 0.06bc	0.35 ± 0.02c	0.86 ± 0.11b	0.73 ± 0.04b
Leaf dry weight (g)	1.15 ± 0.09a	1.11 ± 0.06a	0.90 ± 0.04ab	0.70 ± 0.03b	1.00 ± 0.09ab	1.00 ± 0.08ab
Total dry weight (g)	2.84 ± 0.24a	3.05 ± 0.13a	1.77 ± 0.12bc	1.17 ± 0.06c	2.13 ± 0.23b	1.97 ± 0.12b

Table S7. Gas exchange and chlorophyll fluorescence parameters determined in fully-expanded leaves of *Solanum lycopersicum* cv M82. Measurements were performed at 45 days after germination. Data are means ± se (n = 6 plants). Different letters indicate statistically significant differences (Tukey's test, P < 0.05).

Parameter	M82	M82-*OBV*	*obv-OBV*^{OE}	p_value
A (µmol CO_2 m^{-2} s^{-1})	18 ± 0.78	21 ± 0.85*	20.6 ± 0.49*	**0.04**
g_s (mol H_2O m^{-2} s^{-1})	0.36 ± 0.03	0.38 ± 0.03	0.35 ± 0.02	0.60
E (mmol H_2O m^{-2} s^{-1})	5.37± 0.32 a	4.9 ± 0.16 ab	4.4 ± 0.12 b	**0.00**
WUE_i (µmol CO_2 mol^{-1} H_2O)	51 ± 3.15	55 ± 3.6	59 ± 3.1	0.10
R_{dark} (µmol CO_2 m^{-2} s^{-1})	1.22 ± 0.12	1.24 ± 0.08	1.44 ± 0.11	0.40
g_m (mol CO_2 m^{-2} s^{-1})	0.21 ± 0.02	0.20 ± 0.02	0.17 ± 0.01	0.14
g_m/g_s (mol CO_2 mol^{-1} CO_2)	1.07 ± 0.14	0.96 ± 0.15	0.87 ± 0.11	0.46
C_c (µmol CO_2 mol^{-1} air)	202 ± 8.5 a	171 ± 9.86 ab	154 ± 8.91 b	**0.01**
C_i (µmol CO_2 mol^{-1} air)	292 ± 5.39	283 ± 5.57	278 ± 4.90	0.06
C_i/C_c (µmol CO_2 μmol^{-1} CO_2)	90 ± 10.05	112 ± 14.21	124 ± 11.23	0.06
ETR	133 ± 6.48 b	164 ± 9.63 ab	173 ± 7.85 a	**0.01**
φ PSII	0.29 ± 0.01 b	0.36 ± 0.02 ab	0.38 ± 0.02 a	**0.01**
qP	0.54 ± 0.02 b	0.63 ± 0.03 ab	0.67 ± 0.02 a	**0.01**
V_{cmax_Cc} (µmol CO_2 m^{-2} s^{-1})	97 ± 7.8 b	115 ± 9.44 a	119 ± 5.4 a	**0.007**
J_{max_Cc} (µmol CO_2 m^{-2} s^{-1})	157 ± 7.1 b	182 ± 9.1 a	182 ± 5.3 a	**0.008**
$TPU_{_Cc}$ (µmol CO_2 m^{-2} s^{-1})	8.1 ± 0.3	8.8 ± 0.41	8.8 ± 0.21	0.13
V_{cmax_Ci} (µmol CO_2 m^{-2} s^{-1})	71.7 ± 3.63	78.7 ± 3	81 ± 2.43	0.19
J_{max_Ci} (µmol CO_2 m^{-2} s^{-1})	122 ± 3.57 b	132 ± 5.9 ab	136 ± 3.4 a	**0.03**
$TPU_{_Ci}$ (µmol CO_2 m^{-2} s^{-1})	8.5 ± 0.31 b	9.5 ± 0.43 a	9.4 ± 0.25 ab	**0.03**
Ls	0.25 ± 0.02 b	0.28 ± 0.02 ab	0.30 ± 0.02 a	**0.02**
Lm	0.27 ± 0.03	0.35 ± 0.05	0.39 ± 0.04	0.05
Lb	0.46 ± 0.03 a	0.35 ± 0.03 ab	0.29 ± 0.03 b	**0.006**

* A: photosynthetic CO_2 assimilation rate; g_s: stomatal conductance; E: transpiration; WUE_i: water use efficiency; R_{dark}: dark respiration; g_m: mesophilic conductance; C_c: CO_2 concentration in the chloroplast; C_i: internal concentration of CO_2; ETR: electron transport rate; φ PSII: effective quantum yield of photosystem II; qP: photochemical quenching; V_{cmax}: maximum carboxylation velocity ; J_{max}: maximum electron transport rate; *TPU*: triose phosphate utilization; V_{cmax}, J_{max} and *TPU* were expressed in C_c and C_i basis. Ls: stomatal limitation; Lm: mesophilic limitation; Lb: biochemical limitation.

References

1. K. Hammer, *Die Kulturpflanze*. **32**, 11–34 (1984).

2. R. Milla, C. P. Osborne, M. M. Turcotte, C. Violle, *Trends in Ecology and Evolution*. **30**, 463–9 (2015).

3. R. Milla, J. Morente-López, J. M. Alonso-Rodrigo, N. Martín-Robles, F. S. Chapin, *Proceedings of the Royal Society B*. **281**, 20141429–20141429 (2014).

4. K. Gasparini, J. dos R. Moreira, L. E. P. Peres, A. Zsögön, *Current Opinion in Plant Biology*. **60**, 102006 (2021).

5. A. Zsögön *et al.*, *Nature Biotechnology*. **36**, 1211–1216 (2018).

6. I. J. Wright *et al.*, *Nature*. **428**, 821–7 (2004).

7. T. J. Brodribb, T. S. Feild, G. J. Jordan, *Plant Physiology*. **144**, 1890–8 (2007).

8. L. Sack, N. M. Holbrook, *Annual Review of Plant Biology*. **57**, 361–381 (2006).

9. G. Haberlandt, *Jahrbücher für Wissenschaftliche Botanik*. **13**, 74–188 (1882).

10. R. B. Wylie, *American Journal of Botany*. **39**, 645–651 (1952).

11. I. Terashima, *Photosynthesis Research*. **31**, 195–212 (1992).

12. T. Kenzo, T. Ichie, Y. Watanabe, T. Hiromi, *American Journal of Botany*. **94**, 764–775 (2007).

13. J. H. McClendon, *Plant Physiology*. **99**, 1677–1679 (1992).

14. A. Zsögön, A. C. Alves Negrini, L. E. P. Peres, H. T. Nguyen, M. C. Ball, *New Phytologist*. **205**, 618–626 (2015).

15. C. M. Jones, C. M. Rick, D. Adams, J. Jernstedt, R. T. Chetelat, *American Journal of Botany*. **94**, 935–947 (2007).

16. T. Lin *et al.*, *Nature Genetics*. **46**, 1220–1226 (2014).

17. A. V. Persikov *et al.*, *Nucleic Acids Research*. **43**, 1965–1984 (2015).

18. F. Baile, W. Merini, I. Hidalgo, M. Calonje, *The Plant Cell*. **33**, 2701–2715 (2021).

19. L. Truebestein, T. A. Leonard, *Bioessays*. **38**, 903 (2016).

20. D. Cui *et al.*, *PLoS Genet*. **9**, e1003759 (2013).

21. M. Gallei, C. Luschnig, J. Friml, *Current Opinion in Plant Biology*. **53**, 43–49 (2020).

22. J. Truskina *et al.*, *Nature*. **589**, 116–119 (2021).

23. M. Sagar *et al.*, *Plant Physiology*. **161**, 1362–74 (2013).

24. L. Sack, C. Scoffoni, *New Phytologist*. **198**, 983–1000 (2013).

25. S. A. M. McAdam *et al.*, *Plant physiology*. **175**, 351–360 (2017).

26. T. N. Buckley, L. Sack, M. E. Gilbert, *Plant Physiology*. **156**, 962–973 (2011).

27. K. Kawai, R. Miyoshi, N. Okada, *Trees*. **31**, 1–11 (2017).

28. M. A. Zwieniecki, T. J. Brodribb, N. M. Holbrook, *Plant Cell & Environment*. **30**, 910–921 (2007).

29. C. Aybar *et al.*, *Hydrological Sciences Journal*. **65**, 770–785 (2020).

30. D. Nikolopoulos, G. Liakopoulos, I. Drossopoulos, G. Karabourniotis, *Plant Physiology*. **129**, 235–243 (2002).

31. C. Bellasio, M. R. Lundgren, *New Phytologist*. **212**, 485–496 (2016).

32. M. A. M. Barbosa *et al.*, *Plant, Cell & Environment*. **42**, 1575–1589 (2019).

33. A. Baresch, C. Crifò, C. K. Boyce, *New Phytologist*. **221**, 628–639 (2019).

34. J. Hu, A. Israeli, N. Ori, T. Sun, *The Plant Cell*. **30**, 1710–1728 (2018).

35. M. Arsic *et al.*, *Plant Physiology*. **183**, 1472–1483 (2020).

36. T. Murashige, F. Skoog, *Physiologia Plantarum*. **15**, 473–497 (1962).

37. S. Purcell *et al.*, *The American Journal of Human Genetics*. **81**, 559–575 (2007).

38. S. D. Turner, "qqman: an R package for visualizing GWAS results using Q-Q and manhattan plots" (2014), p. 005165.

39. F. Hahne, R. Ivanek, *Methods Mol Biol*. **1418**, 335–351 (2016).

40. R. C. Edgar, *Nucleic Acids Research*. **32**, 1792–1797 (2004).

41. S. Capella-Gutiérrez, J. M. Silla-Martínez, T. Gabaldón, *Bioinformatics*. **25**, 1972–1973 (2009).

42. M. N. Price, P. S. Dehal, A. P. Arkin, *PLOS ONE*. **5**, e9490 (2010).

43. V. Lefort, J.-E. Longueville, O. Gascuel, *Molecular Biology and Evolution*. **34**, 2422–2424 (2017).

44. S. Guindon *et al.*, *Systematic Biology*. **59**, 307–321 (2010).

45. P. S. Hosmani *et al.*, "An improved de novo assembly and annotation of the tomato reference genome using single-molecule sequencing, Hi-C proximity ligation and optical maps" (2019), p. 767764.

46. M. Karimi, D. Inzé, A. Depicker, *Trends in Plant Science*. **7**, 193–195 (2002).

47. L. E. Pino *et al.*, *Plant Methods*. **6**, 23–23 (2010).

48. K. Edwards, C. Johnstone, C. Thompson, *Nucleic Acids Research*. **19**, 1349–1349 (1991).

49. M. Expósito-Rodríguez, A. A. Borges, A. Borges-Pérez, J. A. Pérez, *BMC plant biology*. **8**, 131–131 (2008).

50. E. J. Oliveira *et al.*, *Protoplasma*. **254**, 2017–2034 (2017).

51. B. Genty, J.-M. Briantais, N. R. Baker, *Biochimica et Biophysica Acta (BBA) - General Subjects*. **990**, 87–92 (1989).

52. K. Oxborough, N. R. Baker, *Photosynthesis Research*. **54**, 135–142 (1997).

53. A. Melis, M. Spangfort, B. Andersson, *Photochemistry and Photobiology*. **45**, 129–136 (1987).

54. P. C. Harley, F. Loreto, G. Di Marco, T. D. Sharkey, *Plant Physiology*. **98**, 1429–1436 (1992).

55. C. D. Muir, M. À. Conesa, E. J. Roldán, A. Molins, J. Galmés, *New Phytologist*. **213**, 1642–1653 (2017).

56. S. P. Long, C. Bernacchi, *Journal of Experimental Botany*. **54**, 2393–2401 (2003).

57. G. Grassi, F. Magnani, *Plant, Cell and Environment*. **28**, 834–849 (2005).

58. M. Rodeghiero, Ü. Niinemets, A. Cescatti, *Plant, Cell and Environment*. **30**, 1006–1022 (2007).

59. T. Ulmasov, Z. B. Liu, G. Hagen, T. J. Guilfoyle, *Plant Cell*. **7**, 1611–23 (1995).

60. W. B. Silva *et al.*, *Plant Physiology*. **176**, 2904–2916 (2018).

61. A. P. Rigui, M. Gaspar, V. F. Oliveira, E. Purgatto, M. A. M. de Carvalho, *Annals of Botany*. **115**, 1163–1175 (2015).

62. D. R. Lewis, G. K. Muday, *Nature Protocols*. **4**, 437–451 (2009).

63. D. H. Chitwood *et al.*, *Plant Cell*. **25**, 2465–81 (2013).